Liquid Drop Actuation by Photoelectrowetting

by

Cesar Palma

A dissertation submitted in partial fulfillment
of the requirements for the degree of
Doctor of Philosophy
(Applied Physics)
in The University of Michigan
2017

Doctoral Committee:

Associate Professor Robert David Deegan, Co-Chair
Associate Professor Çagliyan Kurdak, Co-Chair
Professor David R. Dowling
Associate Professor Lu Li

Cesar Palma Aguilar

czarv@umich.edu

ORCID iD: 0000-0002-1962-9672

ACKNOWLEDGEMENTS

I would like to thank Robert Deegan for lending his expertise to this research project. Through his mentorship I have absorbed a certain ethos, one that has allows tackling complex and difficult problems in simple and efficient ways. I am grateful for the assistance of many staff members at the Lurie Nanofabrication Facility. Pilar Herrera Fierro, Nadine Wang and Tom Latowski in particular provided invaluable help and training in several cleanroom processes that my project relied on. I would also like to thank the members of my dissertation committee for their feedback on this work. Conversations with Prof. Çagliyan Kurdak over the years helped to clarify device physics concepts related to my project. Stephan Weiss was someone I could turn to for assistance and advice on experimental setups. I thank my friends and family for their support.

This research was supported by DARPA.

TABLE OF CONTENTS

LIST OF FIGURES

Figure

ABSTRACT

In electrowetting an electric potential is applied between a droplet of electrolyte and a conductor separated by an insulator. The repulsion of like charges deforms and spreads the droplet over the insulator until capillary and electric forces are in equilibrium. Photoelectrowetting is a light-triggered version of electrowetting where the conductor is replaced by a moderately-doped semiconductor. The electrolyte-insulator-semiconductor stack resembles a metal-insulator-semiconductor capacitor, which has the special property that the amount of charge that can be injected into it increases when exposed to light. Thus in photoelectrowetting the exposure of light spreads the droplet further than in unilluminated conditions. In this thesis a scheme is presented for moving drops on a surface using photoelectrowetting.

In order to understand photoelectrowetting I conducted a study of electrowetting with semiconductors. Devices were constructed using moderately-doped p-type silicon wafers ($N_a = 8.6 \times 10^{14}\,\mathrm{cm}^{-}3$) coated with a bilayer composed of thermal oxide (100 nm) and teflon (265 nm). Electric biases ($< 40\,\mathrm{V}$) were applied between droplets of electrolyte (10 µL, 10 mM NaCl) and the silicon wafer, resulting in deformations of the droplet. These changes were quantified with contact angle measurements which varied from 120° at zero bias to 90° at 40 V depending on the conditions of the experiment. Three regimes were observed depending on the polarity of the bias and above-bandgap illumination impinging on the droplet, corresponding to the charge regimes of an MIS capacitor: accumulation, inversion and deep-depletion. I present a new model for these wetting changes based on a balance of capillary and electrostatic forces. After accounting for various non-ideal effects, I find that the model agrees with

the data. I demonstrate that it is essential to account for interface traps in our devices ($1.8 \times 10^{11}\,\mathrm{cm}^{-2}$) in the deep-depletion regime, leading to a 33% (4°) correction to the prediction at 40 V. I elucidate the nature of the photoelectrowetting effect and find that contrary to reports in the literature the transition is not reversible by light alone.

In the next phase of my thesis, I demonstrate how photoelectrowetting triggered with a light beam on one side moves the droplet along a surface. Comparable with traditional electrowetting-based devices, I achieve speeds of up to 12 mm/s with 10 µL drops of electrolyte (1 % w/w NaCl) with a surfactant (5 mM NaCl) using an oscillating electric potential composed of an AC bias of magnitude 32.5 Vpp and a DC offset of −7 V cycled at a frequency of 15 kHz and a laser intensity of $40\,\mathrm{mW/cm^2}$ ($\lambda = 660\,\mathrm{nm}$). I measure the speed for varying magnitude and frequency of the applied bias, laser intensity, droplet size and fluid viscosity. The optimal cycling frequency is set by competing effects: on the low frequency side (< 15 kHz) the speed is limited by the migration of carriers from the illuminated to the non-illuminated regions under the drop, and on the high frequency side (> 15 kHz) the speed is limited by the intensity of the laser. I present a model for the speed incorporating these effects that compares favorably with the data.

I also present results of simulations of the minority charge carrier concentrations in depletion regions. These exhibit self-similarity in space and time. The front of the concentrations follows a power law in time with an exponent that depends on the dopant concentration. Predictions from the power laws compare favorably with experiment.

CHAPTER I

Introduction

Electrowetting is the phenomenon wherein the application of an electric potential to a liquid droplet resting on a substrate causes it to spread. In this thesis I report a new method for moving microliter-sized droplets on a solid surface using photoelectrowetting, a light triggered variant of electrowetting on a semiconductor substrate. First, I develop the theory for this phenomenon and show that it compares well with my experiments for static droplets. Next I show with experiments that photoelectrowetting can actuate translational motion of a droplet, and I measure the dependence of the speed on various control parameters. Lastly, I develop a model to predict the maximum speed as function of the control parameters, and show that it compares favorably with the model. In this introductory chapter, I give the motivation for this research effort, summarize the state-of-the-art in this field, and give a pedagogical introduction to the background physics used in the rest of this thesis.

1.1 Motivation

Microfluidics is the science of manipulating small quantities of fluids. The field has grown rapidly in recent decades due to a wide range of potential technological and scientific applications [Whitesides, 2006]. Target areas include medicine [Yager et al., 2006], display technology [Hayes and Feenstra, 2003], screening for hazardous

Figure 1.1: A glucose meter that allows diabetics to monitor the sugar content of their blood. A drop of blood is obtained with a lancet and placed on a wicking strip that is analyzed by the meter.

substances [Scholten et al., 2014], optics [Berge and Peseux, 2000] and biological research [Balagaddé et al., 2005]. This diversity of applications reflects the manifold advantages and possibilities that arise with miniaturization, including reduced usage of reagents and shortened processing times.

Perhaps the most intriguing prospect is large scale integration of processes on a single device, termed *lab-on-a-chip*. Early in the 20th century, computation required the construction and operation of enormous, expensive, and power hungry machines like ENIAC[1]. The transistor replaced the vacuum tube and mitigated some of these burdens. However it was the *integrated circuit*, the development of methods for efficiently constructing circuits with large numbers of transistors, that truly started a revolution in the way we live our lives and do science. Integrated circuits were orders of magnitude cheaper, faster, and smaller than their counterparts made from discrete components. An analogous revolution is envisioned for the integration and automation of laboratory processes in chemistry and the life sciences on small, fast, and cheap devices [Thorsen et al., 2002].

[1]ENIAC's dimensions were roughly 100 ft x 8 ft x 3 ft and it weighed 30 tons. It consumed 150 kW and it had 5,000,000 hand-soldered joints. It cost approximately $7,000,000 in 2017 US dollars.

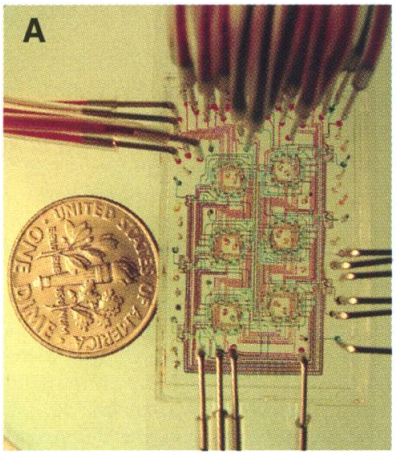

Figure 1.2: A microfluidic chemostat. The device studies the growth of microbial populations in response to varying concentrations of nutrients. From Balagaddé et al. [2005].

The ensuing compactness alone raises game-changing possibilities. Processes that currently require bulky stationary equipment would become mobile. In medicine such portability could substantially increase diagnostic capabilities in remote rural locations [Yager et al., 2006] as well as aid in the treatment of patients requiring continuous treatment, for instance dialysis [Ronco et al., 2011]. In the context of security, screening for chemical or biological weapons could be accomplished with inconspicuous handheld devices [Scholten et al., 2014]. The ability to conduct many experiments simultaneously would also be a great aid in the drug discovery process [Dittrich and Manz, 2006].

In the following section I review current approaches to microfluidic devices and operations.

1.2 Overview of Existing Technologies

Several devices have been applied successfully in particular contexts but most have drawbacks that limit their potential as a true lab-on-a-chip platform. In many devices the reagents flow through predefined channels, which are fundamentally limited

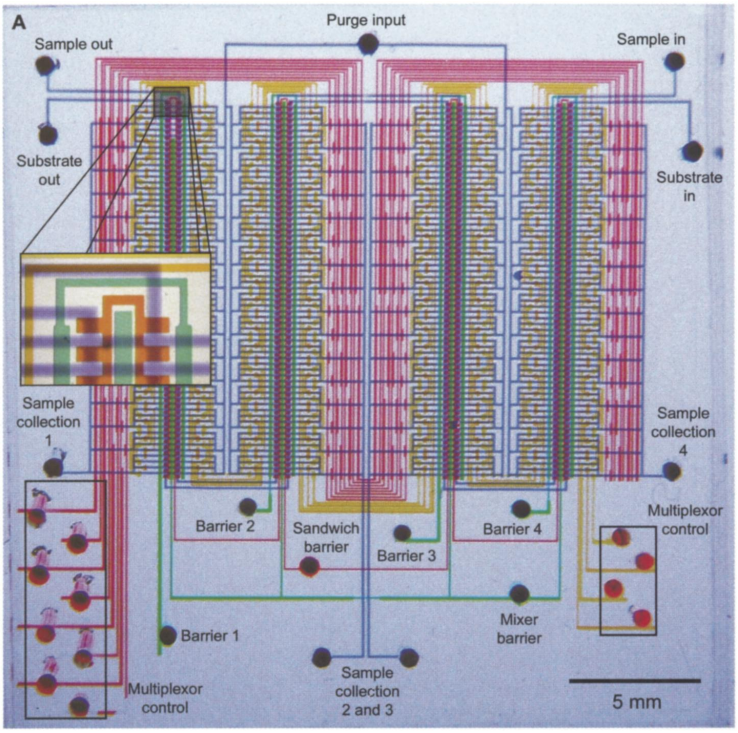

Figure 1.3: A microfluidic comparator made with soft lithography on PDMS. From Thorsen et al. [2002].

because these paths cannot be changed once built. For instance, the addition of a substance to a given process would necessitate the construction of a new device with an additional channel. Moreover these devices typically actuate fluids with pressure by mechanical pumps, electroosmotic flow, or wicking, all of which have limitations. The use of pumps increases device bulk which limits the prospects for portability. A reduced device lifetime is also generally expected from the pumps, as these have moving parts. Devices that actuate via wicking can only be used once. Electroosmotic flow (EOF) actuation works by a running a current through the target fluid in order to move it. This actuation scheme results in undesirable electrolysis at the electrodes. Several devices have been built that overcome these limitations with special patterned surfaces but their construction typically entails the use of microelectronic fabrication equipment, making them expensive to construct and tinker with, especially for re-

searchers without access to such equipment. In what follows I give a broad overview of existing devices.

Many of the early devices employed *continuous flow*, where a single fluid streams continuously through predefined channels. The platform comes with characteristic problems. Axial dispersion of chemical species due to the parabolic flow profile near the channel walls is undesirable in certain contexts [Stone et al., 2004]. The very low Reynolds numbers dictate laminar flow regimes that lend to poor mixing in spite of the small dimensions involved [Seemann et al., 2011]. Furthermore, the number of experiments that can be performed in parallel generally increases linearly with the size of the device, so scaling presents a challenge [Teh et al., 2008]. All these issues can be improved with *droplet-based* devices, where reagents are handled as discrete volumes [Seemann et al., 2011]. This approach allows the independent control of each droplet, which serves as an individual microreactor. Multiple experiments can thus be run in parallel without need for a larger device.

A popular platform for microfluidic devices are polydimethylsiloxane (PDMS) devices constructed via soft lithography, thanks in part to the speed with which new prototypes can be built [Whitesides, 2006]. Duffy et al. [1998] pioneered the method that creates networks of channels as small as tens of microns wide. A pattern of channels is printed on a transparency using a high resolution printer that is then used as a mask in a lithography setup to create a positive relief of the pattern in photoresist. The devices are then finished by curing PDMS against this master, and then sealing the resulting structure with a glass cover by oxidizing in oxygen plasma. This last step also enables electroosmotic flow in the channel. The elastomeric nature of PDMS allows the construction of *Quake valves*, which restrict the flow in a channel with pressure from an adjacent channel. Figure 1.3 shows a completed PDMS device. Actuation of the fluid through the channels is typically accomplished with a mechanical pump or electroosmotic flow [Anderson et al., 2000].

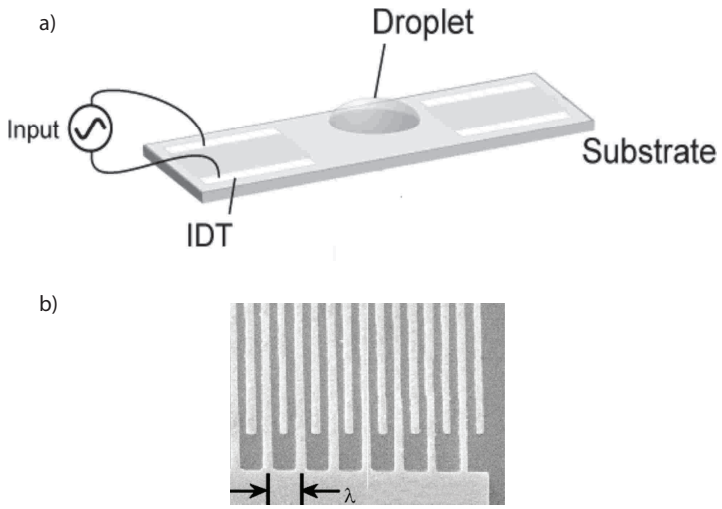

Figure 1.4: SAW device. (a) Device schematic. Application of bias to interdigitated electrodes, here labelled IDT, drives droplet. (b) Closeup of interdigitated electrodes (IDT) patterned on piezoelectric substrate; $\lambda \approx 400\,\text{nm}$. From Yeo and Friend [2009].

Translation of individual droplets has been accomplished in several ways. Yeo and Friend [2009] achieved actuation with surface acoustic waves (SAW). The devices are constructed by depositing interdigitated electrode patterns on a piezoelectric substrate. Application of a sinusoidal (AC) bias to the electrodes generates surface acoustic waves that in turn push the droplets (figure 1.4).

Carrilho et al. [2009] developed low cost paper-based microfluidic devices, constructed by depositing hydrophobic wax patterns on a paper substrate using a commercial wax printer. The wax is then melted into the paper using a hot plate to form wetting barriers. Passive flow by wicking is confined to areas of the substrate free of wax. Figure 1.5 shows one such device.

Darhuber et al. [2003] demonstrated a droplet actuation scheme with thermally induced surface tension gradients (figure 1.6). Surface tension decreases with increasing temperature and this temperature gradient across a droplet will drive a flow towards the colder, high tension side. These devices are constructed using photolithography

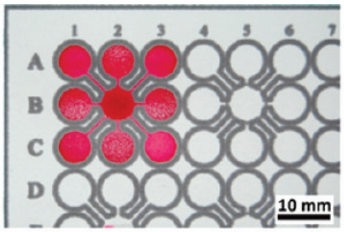

Figure 1.5: Paper-based microfluidic device. This simple device distributes a sample from a central reservoir. From Carrilho et al. [2009].

and physical vapor deposition to form electrical resistors, followed by the deposition of an SiO_2 layer on top. The device has the advantage of being single-sided so that handling and sensing can be accomplished with greater ease.

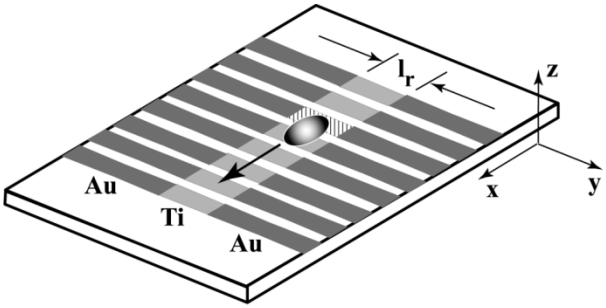

Figure 1.6: Thermocapillary actuation device. The light gray strips depict titanium resistors beneath the surface that locally heat a droplet, driving it towards colder regions. From Darhuber et al. [2003].

Pollack et al. [2000] achieved droplet motion via exploitation of electrowetting-on-dielectric (EWOD). A device schematic is presented in figure 1.7. Application of an electric potential difference between the ground electrode and one of the control electrodes causes the fluid to spread asymmetrically, moving the droplet towards the control electrode. The device was constructed using standard microfabrication technology, including photolithography. A variation on the approach was presented by Chiou et al. [2003, 2008], who achieved droplet locomotion with light by replacing the electrode grid in an EWOD device with a photoconductive amorphous silicon layer.

They observed fluid spreading in response to the simultaneous application of above-bandgap illumination and an electric potential, terming the effect *optoelectrowetting* (OEW). They induced droplet motion by shining light exclusively on one side of the droplet. This technique is notable because the surface is featureless, negating the need to employ photolithography in the construction process.

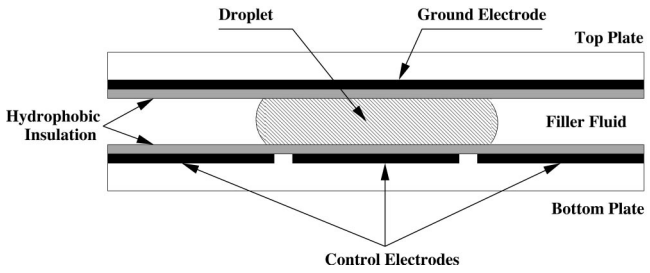

Figure 1.7: Device schematic for actuation of droplets via electrowetting-on-dielectric. From Pollack et al. [2000].

In this work I will explore a new light triggered variant of EWOD for droplet actuation. In contrast to devices where the fluids flow through immutable channels it can direct the motion of droplets in any direction along a surface. As the technique relies exclusively on electrical effects there is no need for mechanical pumps or other failure-prone moving parts. Like the optoelectrowetting approach the surface is featureless, making the device easier to build. This approach presents some material advantages over OEW devices, including an easily deposited and high quality native oxide as insulator, as well as immunity to possible degradation from the Staebler-Wronski effect in amorphous materials.

1.3 Background & Prior Work

1.3.1 Electrocapillarity, Electro-Wetting and Electrowetting-on-Dielectric

A sessile droplet resting on a partially wetting surface makes an angle θ, called the *contact angle*, between the liquid-vapor interface and the solid at the triple phase

line (figure 1.8). The triple phase line, or *contact line*, is defined as the curve where all three phases (solid, liquid and vapor) meet.

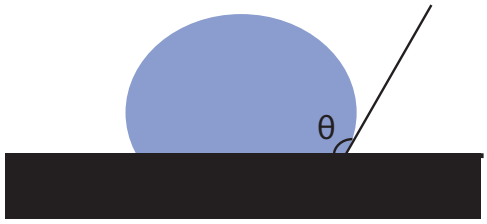

Figure 1.8: The contact angle of a fluid on a partially wetting surface.

The surface tension of an interface is defined as the change in free energy, F, per unit area, A [de Gennes et al., 2004]:

$$\gamma = \left(\frac{\partial F}{\partial A}\right)_{T,V,n} \tag{1.1}$$

where T is the temperature, V is the volume and n the number of molecules. The relationship between θ and γ can be derived from the work done in an infinitesimal displacement of the contact line (figure 1.9). The work $\delta W = (\gamma_{SO} - \gamma_{SL})\, dA - \gamma \cos\theta\, dA$. At equilibrium the free energy is at a minimum hence $\delta W = 0$ and

$$\cos\theta_E = \frac{\gamma_{SO} - \gamma_{SL}}{\gamma} \tag{1.2}$$

a result known as Young's equation [Young, 1805].

Lippmann conducted early important work on the relationship between surface tension and the electric potential difference across an interface. Lippmann showed that it was possible to move the interface of a mercury / aqueous electrolyte in a capillary by the application of an electric potential difference between the liquids [Lippmann, 1875]. Conversely, he found that shifting the location of the meniscus with pressure resulted in a change of the potential.

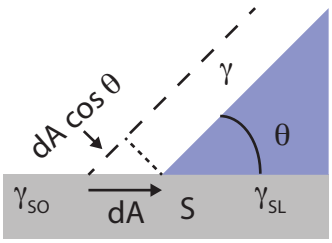

Figure 1.9: Infinitesimal displacement of the contact line. Here θ is the contact angle, γ_{xx} are the interfacial tensions between the phases. The liquid-vapor surface tension is denoted γ for simplicity.

Others [Möller, 1908, Frumkin et al., 1932, Gorodetskaya and Kabanov, 1934, Nakamura et al., 1973] followed his work by measuring the contact angle between mercury or metal electrodes and aqueous solutions while varying the electric potential between them. Beni and Hackwood [1981] introduced the term "electro-wetting" in a scheme for display technology that exploits flow into microchannels in response to an applied potential.

In the works mentioned so far the aqueous solution was in direct contact with the conductors, resulting in a current running through the solution and electrolysis at the electrodes. Berge [1993] introduced a hydrophobic insulating layer between the electrolyte solution and the flat metal conductor (figure 1.10). In the experiments he conducted, termed *electrowetting-on-dielectric* (EWOD), he observed a reduction of the contact angle in response to the application of a potential difference between the metal and the droplet. This reduction occurred simultaneously with an increase in the area of the solid/fluid interface. At moderate voltages, the contact angle follows the Young-Lippmann equation [Mugele and Baret, 2005]:

$$\cos\theta = \cos\theta_E + \frac{c}{2\gamma}V^2 \tag{1.3}$$

Here θ_E is the equilibrium contact angle at zero bias defined by Young's equation, γ is the surface tension of the solid-fluid interface, V is the applied potential for a

constant bias (DC) and c is the capacitance per unit area, $c = Q/(VA) = \epsilon/d$ where Q is the total positive charge, A is the area under the drop, ϵ is the permittivity of the insulator, and d its thickness.

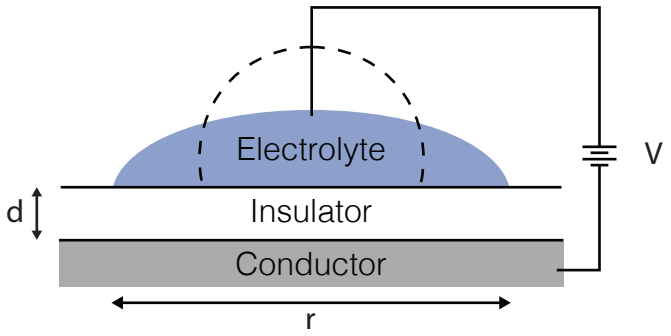

Figure 1.10: Classic electrowetting-on-dielectric. Dashed line depicts shape of the droplet prior to application of the electric potential. Not to scale, r $\approx$ 1 mm and d $\approx 1\,\mu$m.

The phenomenon is closely related to the well-known experiment wherein a slab of dielectric is pulled into the space between two conductors connected to a battery [Jackson, 2007]. The experiment is depicted in figure 1.11. Polarization charges in the fringe fields of the capacitor experience a force pulling the slab inward. By Newton's third law the conductor plates themselves experience an equal and opposite force to the force on the slab. In the case of liquid conductors this force deforms the liquid to cover more of the dielectric. This is the spreading phenomenon observed in electrowetting.

The Young-Lippmann equation can be derived in a similar manner to Young's relation (eqn. 1.2). The addition of a battery introduces a contribution to the free energy from the electric field. Hence, $\delta W = (\gamma_{SO} - \gamma_{SL})\, dA - \gamma \cos\theta\, dA - (\partial U/\partial A)_{T,V,Q}\, dA = 0$, where $U = \frac{1}{2}\int d^3x\ \epsilon E^2$. Young's relation with electric fields, as in electrowetting,

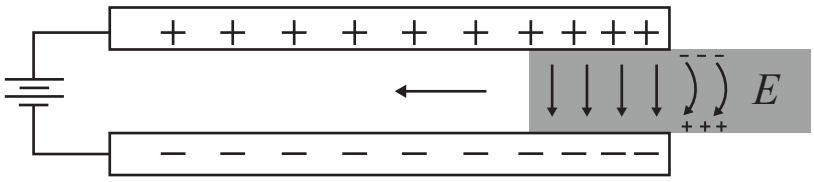

Figure 1.11: A dielectric slab, shown in gray, being sucked into the electric field of a parallel plate capacitor. Polarization charges in the fringe field are responsible for the force.

becomes:

$$\cos\theta = \frac{\gamma_{SO} - \gamma_{SL}}{\gamma} - \frac{1}{\gamma}\left(\frac{\partial U}{\partial A}\right)_{T,V,Q} = \cos\theta_E - \frac{1}{\gamma}\left(\frac{\partial U}{\partial A}\right)_{T,V,Q} \tag{1.4}$$

In electrowetting experiments the thickness of the insulator is typically of the order of microns or less, droplet volumes are typically microliters, and their radii are typically millimeters. For this geometry $U = Q^2/2cA$ follows from the infinite parallel plates approximation for the charge distribution [Jackson, 2007], neglecting fringe fields. Differentiating yields $\partial U/\partial A = -cV^2/2$ and together with equation 1.4 gives equation 1.3.

The electric field decays into the electrolyte liquid over a characteristic length known as the Debye length. The parallel plate approximation for the charge distribution will be accurate if the Debye length is much smaller than the thickness of the insulator. The assumption is appropriate in typical electrowetting experiments, as will be demonstrated in chapter II.

Electrowetting also occurs with a sinusoidal (AC) bias [Mugele et al., 2005]. When the frequency exceeds a threshold the contact line can no longer keep up with the changing potential and instead responds to the time-averaged force. For millimeter sized drops of aqueous electrolyte this threshold frequency is typically a few hundred hertz. With an AC bias the Young-Lippmann equation still applies if V is replaced

by the root mean squared value of the potential, $V_{RMS} = V_{AC}/\sqrt{2}$, where V_{AC} is the amplitude of the applied bias. The Young-Lippman equation remains valid so long as the electric field is confined to the insulator, in keeping with the parallel plate approximation. However it takes a finite amount of time to charge the capacitor formed by the conductive-liquid/insulator/metal stack. As the frequency of the AC bias increases, it's period decreases. When this period approaches the time necessary to charge the capacitor the electric field begins to penetrate into the liquid. The parallel plate approximation used above for U is inappropriate then and the Young-Lippmann equation with V_{RMS} no longer applies at these high frequencies.

Empirically it has been found that at large values of the potential, both in DC and AC, the contact angle saturates, i.e. no further reduction is observed with increasing voltage. The phenomenon remains the subject of investigation [Chevalliot et al., 2012, Chen and Bonaccurso, 2014].

1.3.2 Wetting and Electrowetting Dynamics

The contact line of a sessile droplet is the curve at which all three phases (solid, liquid and vapor) meet. While Young's law says the line will move when a force is applied, in practice no motion occurs below a certain threshold for the force. The physical origin of pinning is the force needed for the contact line to surmount patches of greater or lesser wettability. Figure 1.12 shows the distortions of the contact line when such a patch is met.

The most important feature of contact line pinning is illustrated in figure 1.13. In the first scenario liquid is slowly removed from the drop. Experiments show that the contact line remains stuck and the contact angle decreases until reaching a lower threshold called the receding contact angle θ_r. Thereafter, the contact line will move inward maintaining an angle equal to θ_r. In second scenario liquid is slowly injected into the drop. Like the first scenario, the contact line is stuck. The contact angle

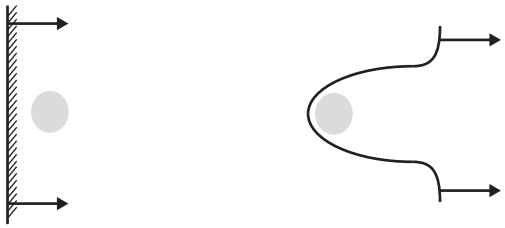

Figure 1.12: Physical origin of pinning. As a liquid attempts to recedes a patch of greater wettability (gray patch) prevents the line from receding and distorts the contact line.

increases up until it reaches the advancing contact angle θ_a and only then does the contact line move. In general, we will observe $\theta_a > \theta_r$. This phenomenon is referred to as *contact angle hysteresis*.

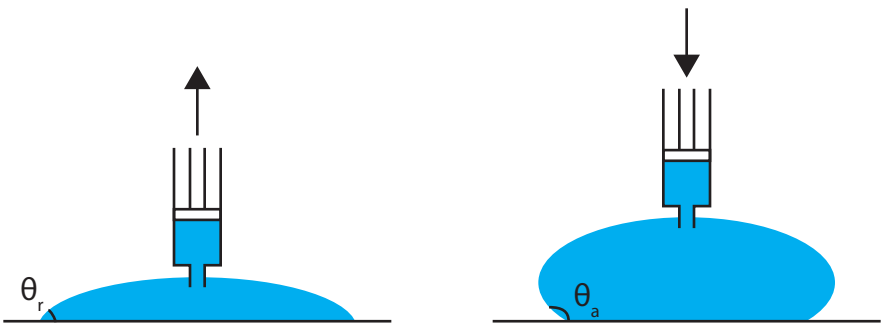

Figure 1.13: Contact angle hystersis, after de Gennes et al. [2004]. Left: fluid is being pumped out of small puddle making a contact angle θ_r to the solid. Right: fluid is being pumped in to a small puddle, making a contact angle θ_a to the solid. Note that $\theta_a > \theta_r$.

The effect of pinning on electrowetting is that no spreading is observed below a threshold voltage and that θ_E in equation 1.3 must be replaced with θ_a or θ_r, depending on whether the voltage is increasing or decreasing, respectively [Gupta et al., 2011].

Once the contact line is in motion dissipative processes resist its motion. The no-

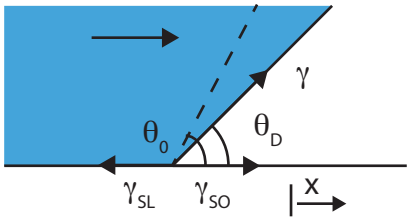

Figure 1.14: Close-up of moving contact line in surface with and without pinning. Dashed line depicts fluid profile in a clean surface with no pinning. Arrows depict force of surface tension for each interface.

slip boundary condition in classical hydrodynamics is problematic. Huh and Scriven [1971] found that the force from viscous stresses diverges at the contact line. Here I present a simplified exposition based on lubrication theory by De Gennes [1985] for creeping flow. The flow profile is parabolic near an advancing contact line, with $u_x = 0$ at the solid/liquid interface (figure 1.15). The velocity of the contact line is the depth averaged speed of the fluid in a cross-section, $U = 1/h \int_0^h dz\, u_x(z)$. Then, $u_x(z) = \frac{3U}{2h^2}(-z^2 + 2hz)$. The rate of viscous dissipation in the cross section is given by [Landau and Lifshitz, 1987]:

$$\int_0^h dz\, \eta \left[\frac{du_x}{dz}\right]^2 = \frac{3\eta U^2}{h} \tag{1.5}$$

Where η is the viscosity of the liquid. Then the net dissipation rate is the integral along the solid/liquid interface:

$$D = \int_{x_{min}}^{x_{max}} \frac{3\eta U^2}{h}\, dx \approx \frac{3\eta U^2}{\theta_D} \ln \frac{x_{max}}{x_{min}} \tag{1.6}$$

In the limit $x \to 0$ the dissipation rate diverges, hence Huh and Scriven [1971]: "not even Herakles could sink a solid." This singularity is resolved by introducing a cutoff length x_{min}, of molecular dimensions, corresponding to different physical mechanisms. Two such mechanisms are the introduction of finite slip at the solid-liquid interface

and a precursor film that wets the surface ahead of the contact line [Bonn et al., 2009]. The parameter x_{max} is a macroscopic cutoff length, the drop's radius in the case of a moving drop. Experiments show $\ln(x_{max}/x_{min})$ lies in the range of 15 to 20 [Marsh et al., 1993, De Gennes, 1985].

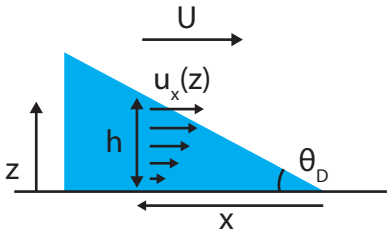

Figure 1.15: Qualitative depiction of velocity profile of fluid in the vicinity of moving contact line as. Profile is of Poiseuille type.

From equation 1.6 we can extract the relationship between the speed of the contact line and the force acting on it. Equating the rate of viscous dissipation to the work done per unit time we have that $D = FU$ hence,

$$F = \frac{3\eta l}{\theta_D} U \tag{1.7}$$

where $l = \ln(x_{max}/x_{min})$.

An alternative to the hydrodynamic theory is the dynamics as a chemical reaction [Blake and Haynes, 1969]. In this "molecular-kinetic" model the force acting on the contact line is related to its velocity according to [de Gennes et al., 2004]:

$$U = U_0 \exp\left(-\frac{E}{kT}\right)\frac{Fa^2}{kT} \tag{1.8}$$

Here $U_0 = a/\tau_0$ where a is a molecular jump length and τ_0 is a microscopic time on the order of 10^{-11} s. E is an energy barrier and kT the usual Boltzmann factor. F is the force. The dynamics of electrowetting have been analyzed within the framework of this theory [Decamps and De Coninck, 2000, Blake et al., 2000]. They examined

the change over time of the radius of the solid/liquid interface in electrowetting experiments and fit the data to $U = F/\xi$. The fit produced a value of $\xi \approx 4\,\mathrm{N\ s/m^2}$, nearly 400 times the viscosity of the fluid.

Le Grand et al. [2005] conducted a series of experiments where drops slid down planes of varying inclination under the influence of gravity (figure 1.16). The capillary number is defined $Ca = \eta U/\gamma$. In these experiments it was observed that for $Ca < 0.01$ the capillary number scaled linearly with the force. Furthermore, it was found that the hydrodynamic theory was most consistent with their data.

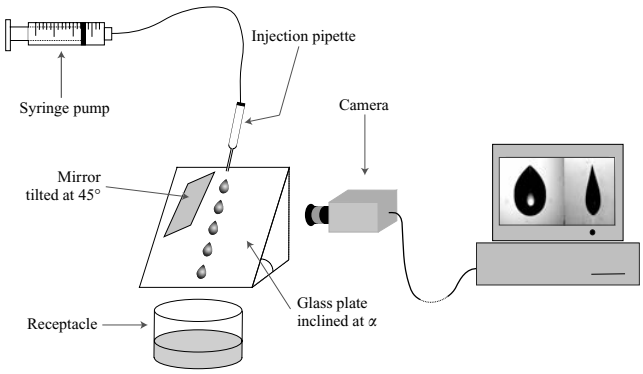

Figure 1.16: Experimental setup for experiments reported in Le Grand et al. [2005]. From Le Grand et al. [2005].

1.3.3 Electrowetting Actuation

Pollack et al. [2000] achieved droplet actuation with electrowetting-on-dielectric. Their device works by inducing electrowetting on one side of the droplet but not the other (figure 1.17) with an array of discrete electrodes alternately electrified. The devices achieved speeds up to 30 mm/s. As noted previously, fabrication of these devices uses photolithography to deposit the electrodes. Figure 1.18 shows a picture of their device.

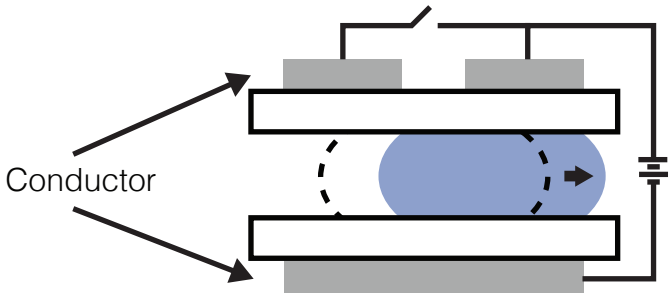

Figure 1.17: Drop actuation via electrowetting-on-dielectric. Dashed lines depict position of the drop prior to application of the potential. Asymmetric application of the electrowetting effect is achieved with a pattern of electrodes. To move the droplet only electrodes on one side of the droplet are energized.

Figure 1.18: Picture of EWOD-based droplet actuation device as seen from above, from Pollack et al. [2000]. The top electrode is made of a transparent material, indium-tin-oxide (ITO). The light gray areas are metal electrodes. The transparent water droplet is on the left, delineated by its glint. The electrode pitch is 1.5 mm

1.3.4 Photo-Electrowetting

Arscott [2011] replaced the conductor in the classic EWOD structure with crystalline silicon (figure 1.19). The electrical conductivity of silicon depends on the intensity of illumination impinging on it. Arscott observed light-induced electrowetting that he termed *photoelectrowetting*. In the first stage of the experiment an electric potential difference was applied between the droplet and silicon wafer in the dark. As with classic EWOD, the liquid spreads. Next, while maintaining the bias, illumination was applied to the drop which caused the drop spread further. The effect could

be reversed by removing the light. The droplet "popped up," in Arscott's own words.

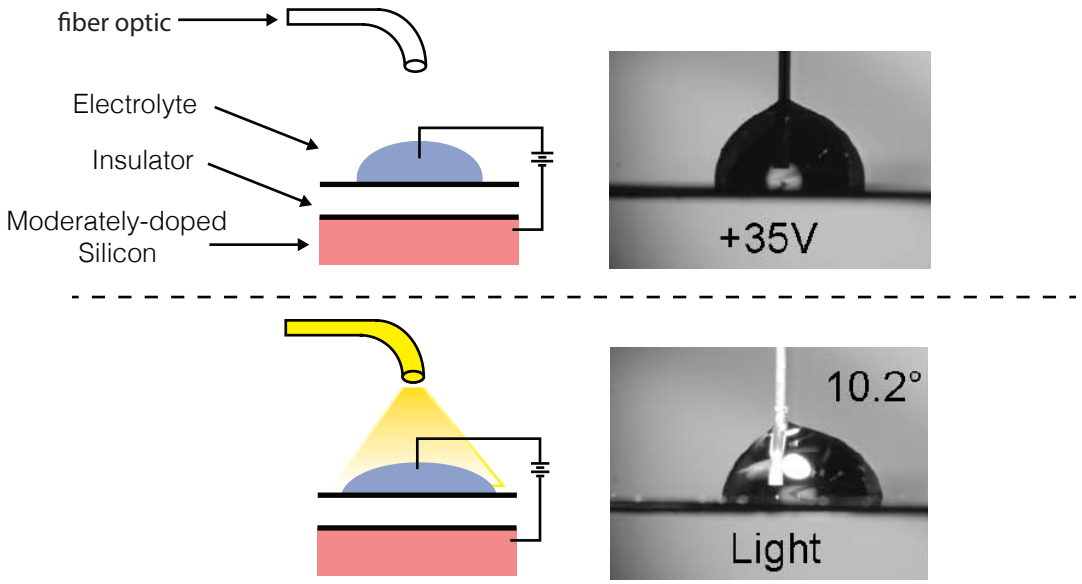

Figure 1.19: The Photoelectrowetting effect. Top: In the first stage of the experiment the potential is applied and an initial wetting transition takes place. Bottom: In the second stage intense light is applied and a second wetting transition takes place. Pictures show the droplet at end of each stage. The change in the contact angle in response to light is noted in the second stage picture. Pictures from *Arscott, 2011*.

As demonstrated by the EWOD-based devices in Pollack et al. [2000], introducing an electrically controlled asymmetry of wetting produces motion of the center of mass of the droplet parallel to the surface. Since photoelectrowetting occurs in response to the presence of light, this raises the intriguing question of whether it is possible to induce droplet motion by introducing an asymmetry in the light pattern shining on the drop? Figure 1.20 presents such a scheme. The main goal of this thesis is to show how this technique can be realized and demonstrate that we are able to induce droplet motion.

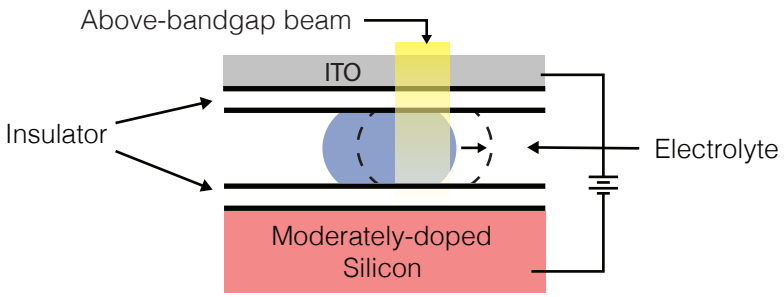

Figure 1.20: Proposed actuation scheme based on the photoelectrowetting effect. Dashed lines depict future position of the droplet. The upper electrode is a conductive transparent material, indium-tin-oxide (ITO).

1.3.5 The Optoelectrowetting Approach

The project undertaken in this thesis shares some similarities with the work presented in Chiou et al. [2008] and Pei et al. [2010] who incorporated an undoped amorphous silicon layer in the EWOD stack. They observed light-induced wetting transitions that they termed *optoelectrowetting* (OEW) and exploited the effect to achieve droplet motion. In this thesis I will show that this is a different effect. Chapter III will cover in more detail the advantages of each approach. Our choice of materials make for a device that is easier to fabricate which, as Whitesides [2006] notes, increases the attractiveness of any platform for exploratory research. Here I review optoelectrowetting.

An optoelectrowetting device schematic is presented in figure 1.21. Optoelectrowetting is modeled with the Young-Lippmann equation (eq. 1.3), with c the unit area capacitance of the insulator and V the RMS potential across the insulator only. Note that in general this is different from the applied bias. By voltage divider action,

$$\frac{V_{oxide}}{V_{AC}} = \frac{Z_{oxide}}{Z_{oxide} + Z_{droplet} + Z_{\alpha-Si}} \tag{1.9}$$

Where V_{AC} is the amplitude of the applied bias and $Z_{\alpha-Si}$ is the impedance of the amorphous silicon layer. Application of light decreases the resistance of the amor-

phous silicon layer and hence V is raised and the contact angle is decreased. To achieve droplet motion a beam is shone on one side of the droplet to achieve asymmetric spreading.

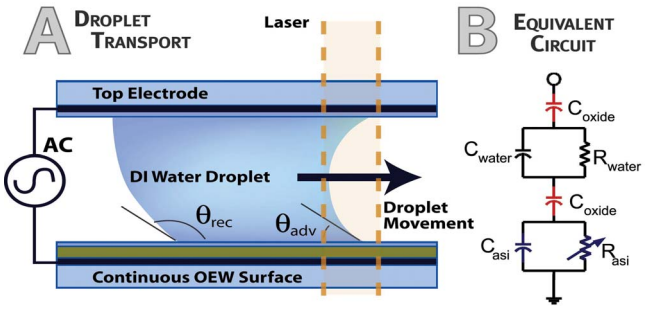

Figure 1.21: Optoelectrowetting device schematic and model, from Chiou et al. [2008]. A. Device schematic. B. Lumped parameter model.

In contrast, as will be shown in chapter II photoelectrowetting transitions cannot be modeled using equation 1.3. Furthermore photoelectrowetting actuation, which will be covered in chapter III, relies on the establishment of the metastable deep-depletion state in the semiconductor on one side of the drop while the illuminated side is inverted. This charge configuration results in a net electrical force that moves the droplet.

1.4 Brief review of Semiconductor Device Physics

In his early investigations Arscott proposed a model for his observations whereby the Young-Lippmann equation (eq. 3.1) dictates the contact angle with the parameter c now a function of the applied bias and the illumination intensity impinging on the photoconductor, $c = c(V, I)$. Arscott notes that the stack composed of a conductive liquid resting on an insulator separating it from a silicon wafer closely resembles the device known as the *metal-insulator-semiconductor* (MIS) *capacitor*. Hence he conjectured, incorrectly as I will show, that c in equation 3.1 should correspond to

the *small-signal* capacitance of this MIS structure. I briefly review here the physics of this important semiconductor device.

1.4.1 Electronic Structure

An important result in the theory of solids is the existence of a band structure for the allowed electronic states in a periodic potential [Bloch, 1929]. Figure 1.22 shows the E-k diagram for silicon [Sze and Ng, 2007], a graph of the available energy states for an electron with wavevector k. An important feature is the existence of a range of energies devoid of electronic states, termed a *bandgap*. The band of states above the gap is termed the *conduction* band and the one below the *valence* band. Electrical conduction is enabled by charge carriers in the upper band, termed *electrons*, and vacancies in the valence band, termed *holes*; the latter act as positively charged particles. In semiconductor devices specific impurities are commonly added in order to increase the number of electrons and holes in the material. This practice is known as *doping*. When a group V element like arsenic is added to the silicon crystal it introduces electronic states with energies close to the conduction band. These states are sufficiently close to the conduction band that they are all nearly thermally *ionized* at room temperature, i.e., they donate an electron to the conduction band, leaving behind a positively charged ion fixed in space. These doped materials are referred to as *n-type* silicon. Similarly, addition of group III elements (e.g. boron) increases the number of holes yielding a *p-type* semiconductor. Electrons in p-type materials and holes in n-type materials are called *minority carriers*. In Arscott's experiments photoelectrowetting was observed only in moderately doped samples, with doping concentration $N \approx 10^{14}$ cm^{-3}.

The number of charges carriers can also be increased through the process known as *photogeneration*, whereby an electron in the valance band absorbs the energy of an incoming photon and is promoted to the conduction band. In order for this to

occur the photon must have energy greater than or equal to the bandgap. In silicon this corresponds to a wavelength of approximately 1.1 µm. There are also momentum considerations. A photon has very little momentum but there is a significant difference in momentum between states at the conduction band minimum and states at the valence band maximum. Transitions between states at different wavevectors are assisted by phonon scattering, which provides the requisite momentum. Hence though a photon may lack sufficient energy to make a direct transition, photogeneration in silicon still occurs for visible spectrum radiation [Sze and Ng, 2007].

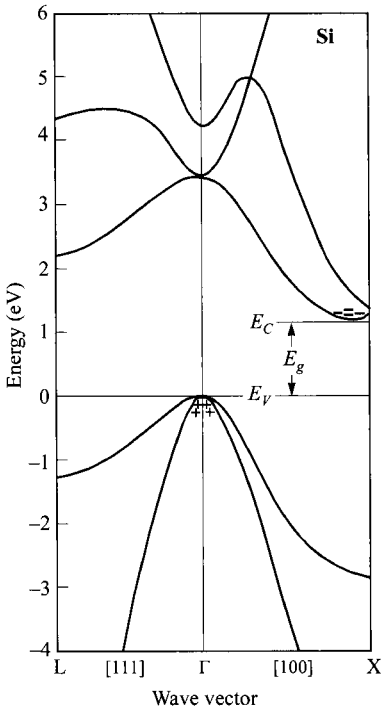

Figure 1.22: Silicon electronic structure. The bandgap is denoted E_g, the top of the conduction band E_c and the top of the valence band E_v. From Sze and Ng [2007].

1.4.2 MIS Charge Distribution

The metal-insulator-semiconductor capacitor is a structure composed of a semiconductor coated with an insulator layer on top of which a metal is deposited (figure

1.23a) [Sze and Ng, 2007]. When the semiconductor is silicon and the insulator is silicon dioxide (SiO_2) the structure is referred to as a MOS capacitor.

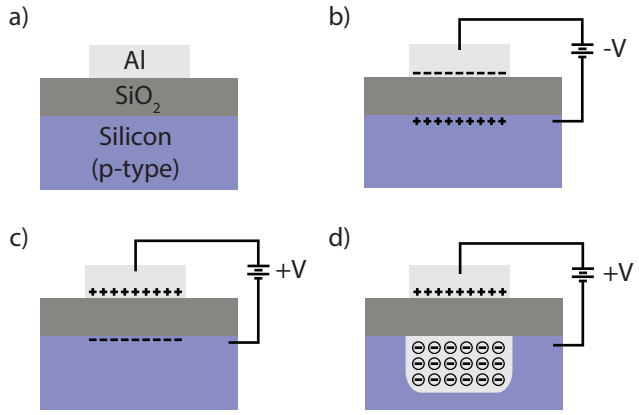

Figure 1.23: The MIS capacitor, simplified charge states. a) Device schematic. Here aluminum is chosen for the gate. b) MIS capacitor in *accumulation*. Electrons are depicted as - and holes are depicted as +. c) MIS capacitor in *inversion*. d) MIS capacitor in the non-equilibrium state *deep depletion*. Here the negative charges are ionized acceptor ions, fixed in space, depicted as $\ominus$

If an electric potential difference is applied between the metal, also called the *gate*, and the doped silicon crystal different charge configurations ensue depending on the polarity of the applied bias and its ramp rate or rate of change. In what follows I will assume that the semiconductor is p-type; for n-type silicon the polarity of the bias and charge are reversed.

A negative bias applied to a p-type crystal will drive holes to the surface of the semiconductor as shown in figure 1.23b. The holes are attracted to the negative charge on the metal. This charge distribution is termed *accumulation*. If a large positive bias is applied, the ensuing charge distribution is more complicated. If the bias is applied slowly, the majority of the charge in the semiconductor will be electrons at the surface of the silicon and the charge configuration is referred to as *inversion* (figure 1.23c). Inversion is the equilibrium state for a large positive bias.

However, if the positive bias is applied rapidly, a metastable configuration develops. The positive charges in the semiconductor are repelled by the positive charges in the metal. If there was a sufficient amount of electrons these would flock to the surface of the semiconductor and create the inversion layer. However, the concentration of electrons in p-type silicon is far smaller than the concentration of ionized dopants, the ones responsible for making the material p-type in the first place. These ionized dopants are fixed in space though, and hence as the holes are repelled they expose what is known as a *depletion region*, a negatively charged region with no mobile charges (figure 1.23d). The electric field penetrates and slowly diminishes into the depletion region due to the presence of the ionized dopants (figure 1.24). The depletion region effectively shields the rest of the semiconductor from the electric field.

Over time the inversion layer will be created via two mechanisms. Electrons in the vicinity of the edge of the depletion region will diffuse into the depletion region and be swept up by the electric field towards the surface. In addition electrons will be promoted from the valence band to the conduction band of the crystal, a process referred to as thermal generation. However both of these processes are relatively slow in device grade silicon wafers and the complete creation of the inversion layer takes on the order of minutes for the large biases involved in photoelectrowetting.

1.4.3 MIS Small-Signal Capacitance

The small-signal capacitance of an MIS capacitor is defined $c = \partial Q/\partial V$, the differential amount of charge gained after an infinitesimal increase in the applied bias. In general this is different from the *net* capacitance $C = Q/V$. From here on I will refer to the small-signal capacitance as simply the capacitance and the quantity $C = Q/V$ as the "net capacitance."

The capacitance can be measured with a setup where an electric potential com-

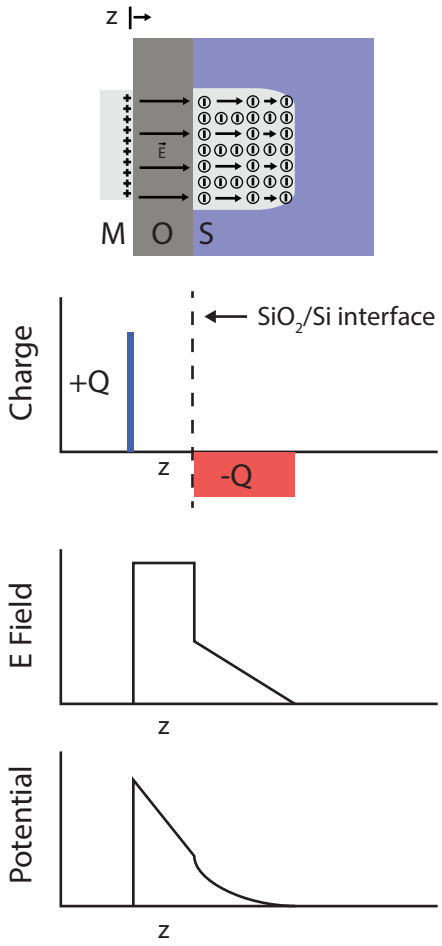

Figure 1.24: MOS electrostatics in deep depletion. Qualitative sketches of the charge, electric field and potential in a p-type MOS capacitor subjected to a large, fast ramp, positive bias.

prised of a ramping bias plus a small AC bias is applied to the gate. The impedance and capacitance can be extracted by measuring the current entering the device. The capacitance will, in general, vary with the charge distribution (accumulation, depletion or inversion) as well as the frequency and magnitude of the small AC bias and the illumination impinging on the device. Representative data of the capacitance as a function of the applied bias, ramp rate, frequency and intensity of illumination for a p-type MOS capacitor are shown in figures 1.26 and 1.27. The capacitance-voltage (CV) characteristics in accumulation are shown in figure 1.27 for negative biases; at

large negative biases the capacitance is simply the capacitance of the dielectric. We can see in figure 1.25a why this is so. Thanks to the high density of holes, an incremental increase in the bias results in an incremental increase in the accumulation layer charge. Because the charge δQ distributes itself directly across both sides of the insulator the capacitance can again be calculated using the parallel plate approximation. The accumulation capacitance then is equal to the net capacitance of the insulator layer.

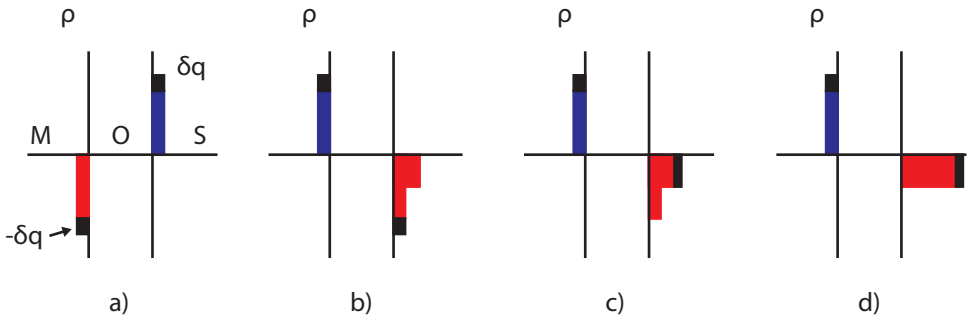

Figure 1.25: Visual depiction of the charges leading to the small-signal capacitance measurements of figures 1.26 and 1.27. The small increments of charge are depicted as small black rectangles. a) Large negative bias (negative biases in figure 1.27). b) Large positive bias at slow ramp and low frequency (labelled "low frequency" in figure 1.26) c) Large positive bias at slow ramp and high frequency (figure 1.26 labelled "high frequency"). d) Large positive bias at fast ramp and high frequency (figure 1.26 labelled "depletion"). Note that in equilibrium there is a small depletion region, depicted in b) and c).

The situation is more complex for positive biases. There are three qualitatively different regimes: low frequencies irrespective of ramp rate, high frequencies at slow ramp rate, and high frequencies at fast ramp rate. First consider a slow ramp rate. If sufficiently slow, the inversion layer is fully formed because there is enough time for the charges to be generated and brought to the surface (figure 1.25b and c). If the frequency of the small AC bias is also sufficiently low then the charge injected into the MOS capacitor goes into the inversion layer and the capacitance is the capacitance of the oxide layer (figure 1.25b). Measurements of the slow ramp, low frequency regime

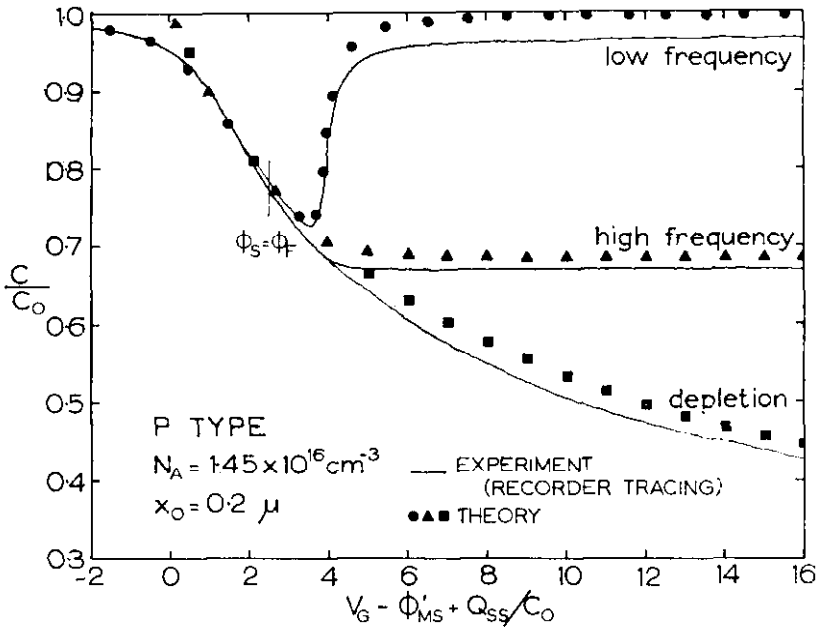

Figure 1.26: CV characteristics for p-type MOS structure. C_o is the capacitance of the oxide layer. Three curves are shown: low frequency, slow ramp high frequency (labelled "high frequency" in the figure) and fast ramp high frequency (labelled "depletion"). From Grove et al. [1965].

are depicted in figure 1.26, labelled "low frequency."

If the frequency of the small AC bias is high though, there is not enough time for mobile charges to be generated, and instead the depletion region increases in depth by a small amount (figure 1.25c). Intuitively we expect the capacitance to be lower for this charge distribution. For a small change in the potential $\delta V = -\int \delta E dx = \delta E_{ave} L$ where L is the distance over which this integral is taken and δE_{ave} is the average field increment over this distance. We can qualitatively compare two scenarios: one where the charge is distributed like a parallel plate capacitor and one where the extra charge in the semiconductor gets added to the end of the depletion region. For a given δV the latter leads to a lower δE_{ave} because L is larger as it now spans the depletion region and the SiO_2 layer. Because $\delta Q \propto \delta E_{ave}$ in the parallel plate approximation [Griffiths, 1999], then we expect $c \approx \delta Q / \delta V$ to be lower in the case when the depletion region

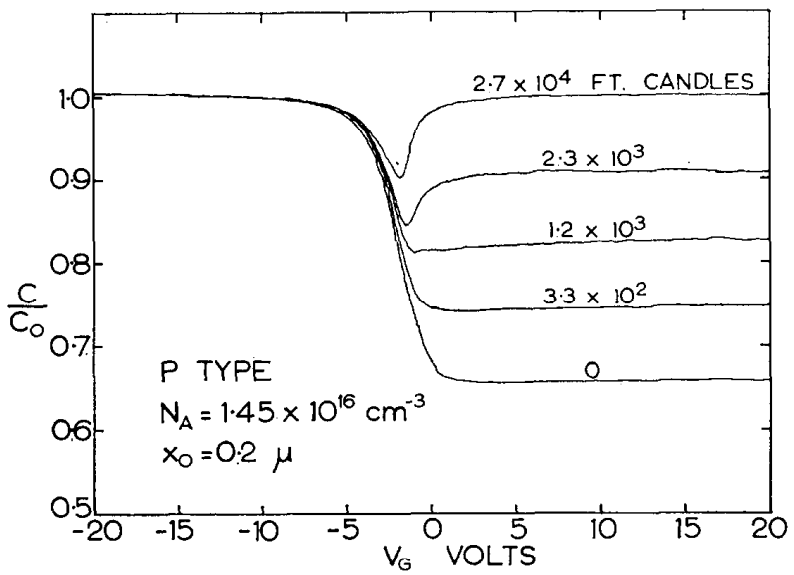

Figure 1.27: High frequency CV characteristics for p-type MOS structure subjected to different illumination intensities of above-bandgap radiation. C_o is the capacitance of the oxide layer. From Grove et al. [1965].

expands, compared to when the charge is added to the inversion layer. Measurements in the slow ramp rate, high frequency regime are depicted in figure 1.26, labelled "high frequency."

Consider now the case of a fast ramp rate, high frequency measurement. In this case the ramp is too fast for the inversion layer to appear at the surface and instead the depletion region extends into the silicon crystal well past its equilibrium depth. Again the high frequency AC bias results in a small packet of charge added at the end of the depletion region (figure 1.25d) except now L is even larger than before and hence δQ is lower than before and the fast ramp, high frequency capacitance is even lower than the slow ramp high frequency capacitance. Measurements of the fast ramp, high frequency regime are depicted in figure 1.26, labelled "depletion."

The impact of illumination with above-bandgap radiation on the capacitance can now be addressed. As discussed previously, such illumination results in photogeneration leading to an increase in the number of electrons and holes in the silicon. Figure

1.27 shows the effect of illuminating the MOS capacitor during a slow-ramp high-frequency CV measurement: with increasing illumination the capacitance increases from the slow-ramp high-frequency value at low illumination to the low-frequency value at high illumination. This change occurs because the photogenerated minority carriers contribute to the formation of the inversion layer. The data shows 2.7×10^4 ft-cd is enough to achieve full inversion in this device. Hence the effect of illumination is to increase the capacitance up to the value of the capacitance of the oxide layer, the maximum attainable value.

1.4.4 Nonideal MIS

The exposition so far assumes that the oxide and the silicon / silicon dioxide interface are free of extraneous charges. This is not generally the case and in fact the presence of various mobile and non-mobile charges strongly impact the capacitance of the MOS structure. I will briefly cover the major effects relevant to my investigations.

1.4.4.1 Work Function Differences

In general there is a difference in the *work function* between the metal and the semiconductor. The work function is the energy needed to remove an electron from a material. As a result of this difference at zero applied bias the net charge on both the metal and the semiconductor is not zero. The net impact on the CV characteristics is to shift the CV characteristics horizontally.

1.4.4.2 Mobile Charges

There are also mobile charges inside the oxide, such as sodium, lithium and potassium ions. A bias applied to the gate of a MOS capacitor induces a migration of ions to the Si/SiO_2 interface resulting in a horizontal shift in the CV characteristics. The effect of these charges can be observed by subjecting a MOS capacitor to

bias-temperature (BT) stressing, where a bias is applied for several hours while the sample is heated. The effect of BT stressing is to deposit a large amount of charge at the interface. If a back-and-forth CV sweep is performed following BT stressing two effects appear: 1) a large horizontal shift in the CV characteristics and 2) hysteresis in the curves. The latter occurs because the interface charge can change appreciably during the sweep itself. Figure 1.29 shows CV measurements of a MOS capacitor before and after BT stressing. Note that this sample is n-type and hence the polarity of the gate in depletion is negative.

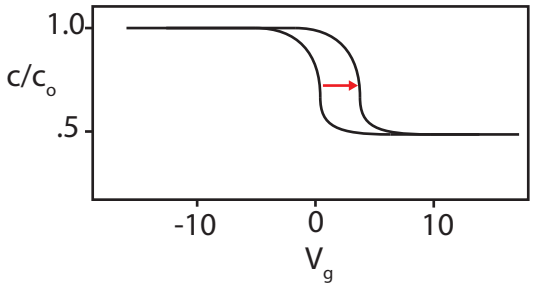

Figure 1.28: Conceptual sketch of combined effect of fixed charge and workfunction differences on MOS CV.

1.4.4.3 Fixed Charges

In addition to mobile charges, there are immobile charges termed *fixed charges*. These are always positive and found within 25 Å of the Si/SiO_2 interface. The origin of these is believed to be excess ionic silicon [Pierret et al., 1996]. Once again the effect of these charges is to shift the CV characteristics horizontally, as in figure 1.28. Because the concentration does not change during a sweep there is no shearing or hysteresis, unlike with the mobile ions.

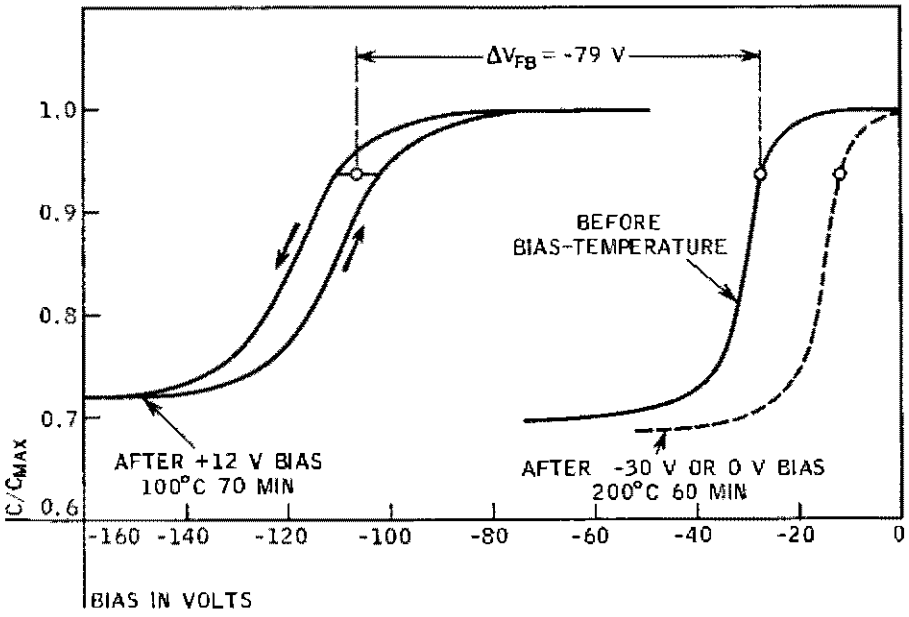

Figure 1.29: High frequency CV characteristics for n-type MOS capacitor subjected to BT stress. Influence of ionic migration in dielectric layer. From Kerr et al. [1964].

1.4.4.4 Interface Traps

Another important nonideal MOS effect is the presence of *interface traps* at the Si/SiO_2 interface. The effect of these on the CV characteristics is depicted in figure 1.30: a horizontal offset to the CV curves and shearing. Evidence supports the hypothesis that these states arise from dangling bonds at the edge of the silicon crystal. These interface traps are located throughout the bandgap and their time constants span the range from microseconds close to the band edges to miliseconds close to midgap. During a photoelectrowetting experiment a large bias is applied that leaves the semiconductor in deep depletion. The practical consequence of these interface traps is that application of a bias that leaves the MIS capacitor in deep depletion will generate a sheet of charge at the interface of the same polarity as the depletion region.

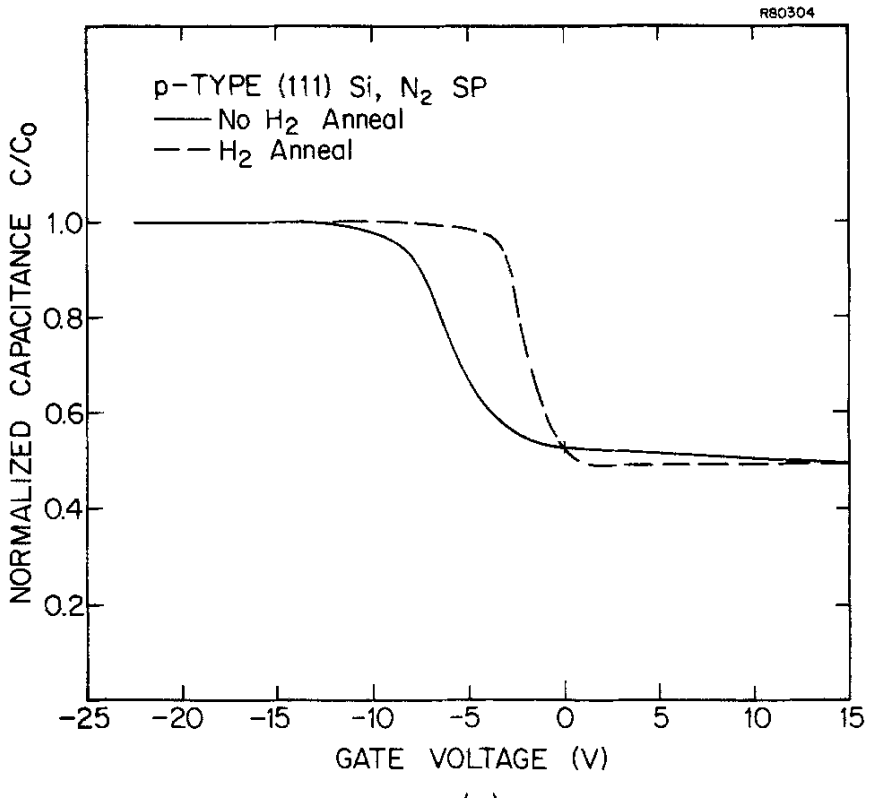

Figure 1.30: Impact of interface traps on the CV characteristics of a p-type MOS capacitor. Dashed line shows CV curve after annealing the sample in H_2, a procedure that minimizes the interface trap density. From Razouk and Deal [1979].

1.4.5 Minority Carrier Dynamics in Depletion Regions

The actuation scheme reported in this thesis introduces an asymmetry in the electrowetting by shining light on only one side of the droplet while a bias is applied (figure 1.20). This results in localized photogeneration and a gradient in the density of minority carriers across the droplet. As we will see in chapter II minority carriers are the source of the photoelectrowetting effect. Hence the asymmetry in the electrowetting can only last as long as the gradient in minority carriers is maintained. However, such a gradient is unstable and electric forces and diffusion homogenize the charge distribution beneath the drop. This migration of minority carriers from the illuminated to the non-illuminated portions of the droplet will turn out to be a

limitation on actuation by photoelectrowetting.

To illustrate the problem consider biasing a p-type MIS capacitor into deep-depletion and then shining intense above-bandgap light on one small section close to the edge, as in figure 1.31. The geometry of this capacitor is similar to that of a droplet in a photoelectrowetting experiment and the electrode is a transparent, conductive material like indium-tin-oxide (ITO). Electron-hole pairs will be generated by the light and subjected to an electric field in the z direction, normal to the surface of the semiconductor. Electrons will come to the surface and holes will be pushed away from it. The charge distribution under the laser beam resembles an inverted MIS capacitor but far away in the non-illuminated portions of the drop there are no electrons yet and so those areas remain in deep-depletion. This scenario is plausible because the gate is a few millimeters wide while the depletion region is only a few micrometers thick. Hence, we generally expect the minority carriers to reach the surface before they reach the un-illuminated edge of the capacitor. From the gradient in the concentration of electrons between the illuminated and non-illuminated portions of the capacitor we expect a diffusive flow.

In addition the charge distribution produces an electric field parallel to the surface driving electrons from the illuminated to the non-illuminated portions of the drop. In the area under the beam the potential at the surface of the semiconductor is close to zero as the semiconductor bulk is grounded in this setup. In contrast, the non-illuminated portions remain in deep-depletion. The potential in the deep-depleted surface will not be close to zero (see figure 1.24). There is an electric field between the bulk, where the potential is zero, and the surface in the un-illuminated portions. Since $\Delta\Phi = -\int \vec{E} \cdot d\vec{x}$, we know that the surface potential must be higher in the un-illuminated than in the illuminated portions of the capacitor and that an electric field exists in the horizontal direction, tangent to the surface. This field will bring electrons from the illuminated to the non-illuminated portions of the MOS capacitor.

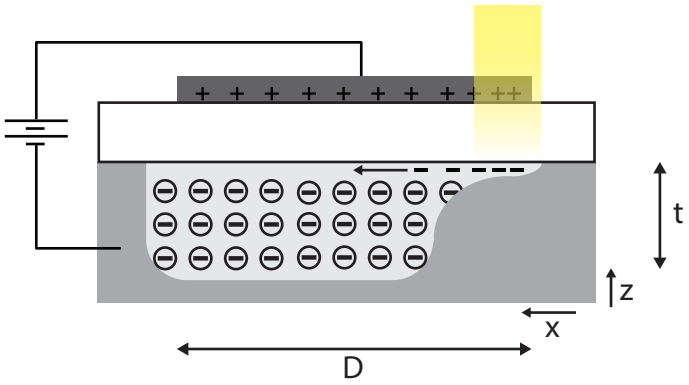

Figure 1.31: Photogenerated carriers in the depletion region of an MIS capacitor, an instant after the electrons have come to the surface. The gate here is made from ITO. The electric field and diffusion will work to equilibrate the concentration of minority carriers across the device. Not to scale, $D \gg t$.

My work investigating the migration of carriers in the depletion region took precedence after early attempts failed to achieve droplet motion. Experiments and numerical simulations were undertaken to tackle this important problem. The dynamics of charge carriers in depletion regions were simulated with the local equilibrium equations [Roosbroeck, 1950]:

$$\epsilon_s \nabla^2 \phi + e(p - n + N) = 0 \tag{1.10}$$

$$\frac{\partial p}{\partial t} + \nabla \cdot J_P = \frac{\partial p}{\partial t} + \nabla \cdot (-\mu_p p \nabla \phi - D_p \nabla p) = 0 \tag{1.11}$$

$$\frac{\partial n}{\partial t} + \nabla \cdot J_n = \frac{\partial n}{\partial t} + \nabla \cdot (\mu_n n \nabla \phi - D_n \nabla n) = 0 \tag{1.12}$$

where ϕ is the electric potential, p is concentration of holes and n is the concentration of electrons. ϵ_s is the permittivity in the semiconductor, e is the fundamental charge, N is the doping concentration and μ_x, D_x correspond to the mobility and diffusion coefficient for each carrier respectively. Equation 1.10 is Poisson's equation with a term, N, that accounts for the concentration of ionized dopants in a depletion region, fixed in space. Equations 1.11 and 1.12 account for the change in the concentration

of carriers in response to electric fields and diffusion. Thermal carrier generation is omitted in these equations because the dynamics of interest happen over timescales much longer than the minority carrier lifetime.

The results of my simulations are presented in chapter IV.

1.5 Outline of this thesis

The first step in my investigations was a reproduction of the photoelectrowetting experiments presented in Arscott [2011]. The results are presented in chapter II. I found that the models previously put forward for photoelectrowetting were flawed. As I will show photoelectrowetting and the other experiments with electrowetting with semiconductors are not modeled by the Young-Lippmann equation (eq. 1.3) with c replaced by the small-signal capacitance of an equivalent MIS capacitor. In order to establish an accurate model it is necessary to examine the equilibrium between capillary and electrostatic forces. In particular, I show that photoelectrowetting is not a "reversible" transition; that is turning off the illumination does not cause the droplet's shape to revert to the pre-illumination state. An expression is derived for the change in the contact angle that takes into account non-ideal MIS effects of fixed charge centers and interface traps. This work was published in *Palma and Deegan* [2015].

Having clarified the nature of the photoelectrowetting transition I moved on to an exploration of how the effect could be exploited to achieve drop motion. These efforts were successful and the results are presented in chapter III. Here I also report on a number of experiments that show how the speed of the motion depends on several experimental parameters including the applied bias, the intensity of illumination and droplet size and liquid viscosity. Based on the results for the forces on the fluid presented in Palma and Deegan [2015], I present a model for these new observations. The results of these investigations were submitted to the journal *Langmuir*.

As I will demonstrate in chapter III a limiting problem for the actuation of droplets via photoelectrowetting is the migration of minority carriers from the illuminated to the non-illuminated regions of the droplet. The net actuation force that drives the droplet comes from the gradient in the concentration of minority carriers between the dark and illuminated portions of the droplet. However, over an effective time τ this gradient softens and disappears because of diffusion and electric forces. These dynamics have a strong impact on the minimum rate of repetition necessary for photoelectrowetting to drive a droplet. In chapter IV I present results based on numerical simulations of the dynamics of minority carriers in depletion regions.

I end this thesis with a conclusions chapter in Chapter V.

CHAPTER II

Static & Quasi-Static Electrowetting on Semiconductors

2.1 Introduction

Electrowetting is a phenomenon wherein the wetting properties of a liquid on a solid substrate are modified by the application of an electric field [Mugele and Baret, 2005]. The effect has been exploited for droplet actuation [Pollack et al., 2000], adjustable lenses [Berge and Peseux, 2000] and electronic displays [Hayes and Feenstra, 2003]. In the basic electrowetting-on-dielectric (EWOD) experimental configuration (figure 2.1) a sessile drop of electrolyte rests on a thin insulator separating it from an electrode, typically a good conductor. Applying an electric potential difference between the drop and the electrode induces spreading and a concomitant reduction of the drop's contact angle θ. This phenomenon is modeled well up until the onset of contact angle saturation [Mugele and Baret, 2005] by the Young-Lippmann equation:

$$\cos\theta = \cos\theta_o + \frac{1}{2}\frac{cV^2}{\gamma_{\mathrm{lv}}} \tag{2.1}$$

Here $V = V_{DC}$ the value of the applied bias if it is DC, or $V = V_{RMS}$ the root-mean-squared value of the applied bias if it is AC and θ_o is the zero-bias equilibrium contact angle. This value is given by Young's equation: $\cos\theta_o = (\gamma_{\mathrm{sv}} - \gamma_{\mathrm{sl}})/\gamma_{\mathrm{lv}}$, where

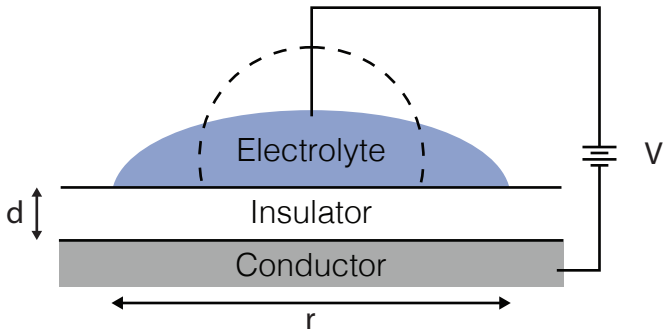

Figure 2.1: Classic electrowetting-on-dielectric. Dashed lined depict shape of the droplet prior to application of the electric potential. Not to scale, r $\approx$ 1 mm and d $\approx$ 1 µm.

γ_{xy} refers to the respective interfacial tensions between the liquid (l), solid (s), and vapor (v). Finally $c = \epsilon/d$, where ϵ is the permittivity of the insulator and d its thickness. As will be shown, however, this formula is only appropriate when the electric field can be calculated using the infinite parallel planes approximation for the charge distribution.

Arscott [2011] observed novel effects when the conductor is replaced by a moderately doped silicon wafer. He conducted DC electrowetting experiments and observed that, unlike the case with a metal electrode, the change in the contact angle was asymmetric with respect to the polarity of the applied bias. Note that in equation 2.1 the potential is squared and hence the prediction for the equilibrium contact angle is independent of the polarity of the bias. He further observed that light induced a reversible wetting transition, a phenomenon he termed *photoelectrowetting*. Here reversibility referred to the fact that the transition was reversed when the illumination impinging on the droplet was removed. Arscott distinguished three electrowetting regimes and associated these with the small-signal capacitance states of a metal-insulator-semiconductor (MIS) capacitor: accumulation, inversion, and depletion. He modeled his results using the Young-Lippmann equation (2.1) with c replaced by the small-signal capacitance (dQ/dV). More recently he revisited these experiments [Arscott,

2013] and proposed a new model where the term $cV^2/2\gamma$ in the Young-Lippmann equation is replaced by E/γ where E is the electrostatic energy per unit area of the solid/liquid interface and γ is the liquid/air surface tension.

Chiou et al. [2008] conducted similar experiments where the electrode in the electrowetting stack was replaced with undoped hydrogenated amorphous silicon. In their experiments these authors applied an AC bias and also observed a light-induced wetting transition that they termed *optoelectrowetting* [Chiou et al., 2003]. They modeled their observations by positing that the change in the contact angle of their droplets was governed by equation 2.1 with $V = V_{i-RMS}$, the RMS potential drop across the insulator as determined by the voltage divider of the insulator's impedance in series with the impedance of the amorphous layer. The conductivity of amorphous silicon in the dark is low and increases when exposed to optical illumination. Hence in the electrowetting experiment when the drop is illuminated V_{i-RMS} increases and the contact angle is reduced.

In this chapter I present experimental and analytical results of electrowetting-on-dielectric with semiconductors surfaces. A modified version of the Young-Lippmann equation is derived to account for the penetration of the electric field into the semiconductor. This new model takes into account non-ideal effects including contact line pinning, interface charges, interface traps, and work function differences. The measurements agree well with this new model. An important finding is that contrary to the results presented in Arscott [2011] photoelectrowetting is non-reversible by light alone because it is a transition from a non-equilibrium to an equilibrium state.

2.2 Theoretical

As Arscott [2011] notes the conductive liquid / insulator / semiconductor (LIS) stack closely resembles the metal-insulator-semiconductor (MIS) capacitor that is the core of the MOS field effect transistor. When a bias is applied to the metal gate

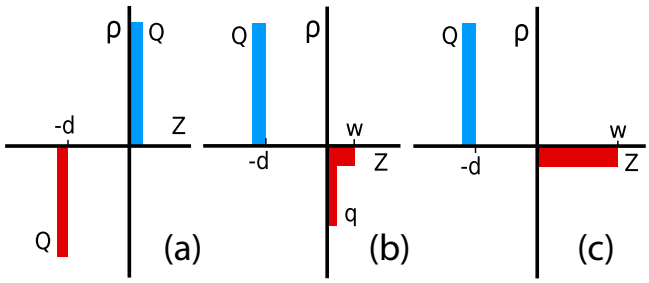

Figure 2.2: Charge distributions for p-type MIS/LIS under: (a) accumulation, (b) inversion and (c) deep depletion. The drop lies on the interval $z < -d$, the insulator $-d < z < 0$, and the semiconductor $z > 0$. Negative charge is depicted in red, positive charge in blue. Note that even in equilibrium the inversion charge distribution still features a depletion region, small when compared to the deep-depletion distribution.

in an MIS device, the corresponding charge distribution can exhibit three distinct equilibrium states depending on the magnitude and polarity of the applied bias relative to the doping type of the crystal: accumulation, depletion and inversion. It is also possible to induce deep-depletion, a non-equilibrium charge distribution formed by rapidly ramping the bias towards inversion. Due to the slow generation rate of minority carriers, the charge distribution remains in the depleted state but with a much deeper depletion width than it would otherwise attain in equilibrium [Nicollian and Brews, 1982]. The charge distribution for these states is depicted in figure 2.2.

In an electrowetting experiment a droplet acquires a charge and changes shape in order to minimize its free energy. The equilibrium contact angle in electrowetting can be computed by minimizing the free energy of the charged droplet with respect to area while holding the temperature, volume, and charge constant. It is also possible to conduct the calculation while holding the electric potential constant but it is then necessary to account for the work done by the DC power source [Griffiths, 1999]. The free energy F has contributions from surface tension and the electrostatic fields. The former is $\gamma_{\mathrm{sl}}A - \gamma_{\mathrm{sv}}A + \gamma_{\mathrm{lv}}S$ where A is the contact area of the drop and S the area

of the liquid-vapor interface, and the latter is $U = \frac{1}{2}\int d^3x\, \vec{D}\cdot\vec{E}$. Thus,

$$\left(\frac{\partial F}{\partial A}\right)_{V,Q,T} = \gamma_{\mathrm{sl}} - \gamma_{\mathrm{sv}} + \gamma_{\mathrm{lv}}\left(\frac{\partial S}{\partial A}\right)_V + \left(\frac{\partial U}{\partial A}\right)_Q = 0 \tag{2.2}$$

It can be shown [de Gennes et al., 2004] that $\left(\frac{\partial S}{\partial A}\right)_V = \cos\theta$, where θ is again the contact angle of the droplet. It then follows that

$$\cos\theta = \cos\theta_o - \frac{1}{\gamma_{\mathrm{lv}}}\left(\frac{\partial U}{\partial A}\right)_Q \tag{2.3}$$

Using the depletion approximation we calculate $(\partial U/\partial A)_Q$ from a generic charge distribution $\rho(x)$ that includes the charge distributions of fig. 2.2 as special cases:

$$\rho(z) = \frac{Q}{A}\delta(z+d) - \frac{q}{A}\delta(z) - eN(H(z) - H(z-w)) \tag{2.4}$$

where Q is the total charge imposed by an external potential, N is the density of ionized acceptors, e is the elementary charge, w is the width of the depletion region, δ is the delta function, and H is the Heaviside function. Charge neutrality requires $\int dA \int_0^w dz\, \rho(z) = Q$ and hence $w = (Q-q)/(eNA)$. For now, we neglect nonideal MIS effects. This analysis assumes that the Debye length for the electric double layer is much smaller than the thickness of the insulator and hence the charge distribution in the liquid can be approximated as a delta function. For the electrolyte solutions presented here the Debye layer is approximately 4 nm whereas the insulator layers are upwards of 350 nm thick total.

We compute the electric field E using Poisson's equation and eq. 2.4, and then $U = \frac{A}{2}\int_{-d}^{w} dz\ \epsilon E^2$, $\left(\frac{\partial U}{\partial A}\right)_Q$ and $V = \int_{-d}^{w} dz\ E$:

$$\left(\frac{\partial U}{\partial A}\right)_Q = -\frac{\Sigma^2}{2c} - \frac{(\Sigma-\sigma)^3}{3\lambda} - \frac{(\Sigma-\sigma)^2}{2\lambda}\left(\frac{\partial q}{\partial A}\right)_Q \tag{2.5}$$

$$V = \frac{\Sigma}{c} + \frac{(\Sigma-\sigma)^2}{2\lambda} \tag{2.6}$$

where c is the net capacitance of the dielectric per unit area ($c = \frac{\epsilon_i}{d}$ for a single dielectric layer with permittivity ϵ_i), $\Sigma = Q/A$, $\sigma = q/A$, $\lambda = \epsilon_s e N$ and ϵ_s is the permittivity of the silicon crystal.

In accumulation $q = Q$ and eqs. 2.3, 2.5 and 2.6 reduce to eq. 2.1.

$$\cos\theta = \cos\theta_o + \frac{c}{2\gamma_{\mathrm{lv}}} V^2 \tag{2.7}$$

Following a rapid ramp, the semiconductor will be in deep depletion and $q = 0$. In deep depletion then,

$$\cos\theta = \cos\theta_o + \frac{\lambda^2}{3\gamma_{\mathrm{lv}} c^3}\left[-1 - 3\tilde{V} + (1 + 2\tilde{V})^{3/2}\right] \tag{2.8}$$

where $\tilde{V} = c^2 V/\lambda$. We note that eq. 2.8 was reported by Arscott [2013] though their method of derivation is different than our own.

While in deep depletion $q = 0$, but as the electrons thermalize q will rise until the semiconductor is inverted. A small depletion layer will remain in inversion, but our numerical calculations indicate that more than 99% of the electrostatic energy is accounted for by the electric field within the insulators and so $q \approx Q$ and eq. 2.1 is an excellent approximation for the contact angle response in inversion.

The deep depletion state forms because the generation rate of minority carriers is slow in very pure semiconductors such as prime silicon wafers. But shining light of wavelength shorter than the corresponding bandgap energy on a semiconductor rapidly generates minority carriers [Sze and Ng, 2007] and thus greatly accelerates the approach to equilibrium. During an electrowetting experiment the system brought into deep depletion by a step-like change in the bias and then illuminated almost instantly changes to inversion. Thus, the net change in contact angle due to illumination is given by the difference of eqs. 3.1 & 2.8. Note however that the role of light is to drive the system towards equilibrium, and thus the process is not reversible, i.e.

turning off the light will not restore the original deep depletion state.

2.3 Experimental

2.3.1 Device Fabrication

In order to test the predictions (eqs. 3.1 & 2.8) and compare our models to those proposed by Arscott electrowetting devices were fabricated as follows. P-type silicon 4" (100) wafers doped with Boron were procured. The wafers were subjected to the following sequence of steps. A 100 nm layer of silicon dioxide was grown by dry oxidation (125 mins at 1000 °C followed by N_2 annealing at the same temperature for 10 minutes). Trans-LC, a chlorine containing compound, was added during oxidation to neutralize mobile ionic charge. Ohmic contacts were fabricated by removing the oxide from target areas by mechanical abrasion with a diamond scribe, depositing a layer of aluminum by physical vapor deposition through a patterned metal mask, and annealing for five minutes at 500 °C in an Argon atmosphere. Two contacts were fabricated on each device and current-voltage measurements indicated that these were good ohmic contacts. A second insulator film made of teflon was deposited on the oxide by spin coating a 2% (w/w) solution of Teflon AF 1600 solids (DuPont) dissolved in FC-40 (Sigma-Aldrich) for 20 seconds at 500 rpm and 30 seconds at 1000 rpm followed by annealing steps for 15 minutes at 183 °C and 15 minutes at 330°C in a 1 atm N_2 atmosphere. The oxide and teflon layer thicknesses were measured by ellipsometry (Wollam M-2000) to be $d_s = 101$ nm and $d_t = 265$ nm, respectively. Together with the literature values for the permittivities of silicon dioxide ($3.9\epsilon_o$) and Teflon AF ($1.93\epsilon_o$), yields an expected value for c of 5.4×10^{-5} F/m^2.

In addition devices were fabricated to measure the MIS small-signal capacitance, which is a key parameter that determines the change in the contact angle in the early model proposed by Arscott. The same process steps and starting wafers were used

as above except that not all devices were subjected to thermal oxidation. Hence two types of devices were built: one where the insulator was a bilayer composed of teflon on top of SiO_2 and another where the insulator was solely teflon. Finally circular gold contacts 200 Å thick with typical radii of milimeters were deposited via physical vapor deposition on top of the teflon layer. This layer is semitransparent to optical radiation [Axelevitch et al., 2012]. The CV measurement devices are depicted in figure 2.3.

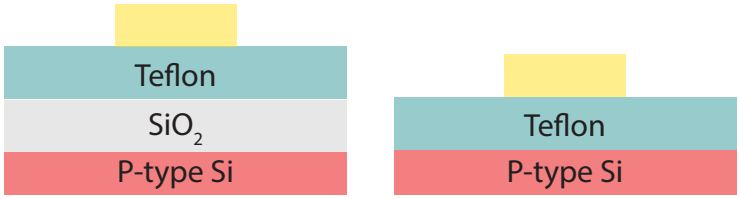

Figure 2.3: Devices built for capacitance characterization. Not to scale.

2.3.2 Ancillary Measurements

In order to rigorously test our models and compare our models to those put forth by Arscott a number of ancillary measurements were conducted. The capacitance was directly measured and it was verified that it exhibits the expected characteristics of a MOS capacitor, including the effect of illumination. We also measured the parameters of the doping concentration (N in equation 2.8) and the surface tension of the fluid (γ_{lv} in equations 3.1 & 2.8).

2.3.2.1 Capacitance

The capacitance measurements were performed using a lock-in amplifier (Stanford SRS-830), a bipolar DC power supply (Keithley 2400 SMU) and a function generator (Agilent 33210A) with a circuit as shown in figure 2.4. The bipolar power supply provides a ramping DC bias V_{DC} while the function generator provides a small AC bias

V_{ss}. The lock-in amplifier measures the phase and amplitude of the current passing through the MIS capacitor, allowing a direct small-signal impedance measurement. The high frequency CV characteristics for devices with a single layer teflon insulator are shown in figure 2.5 in dark and illuminated conditions. The CV curve exhibits the characteristics expected for a MOS capacitor subjected to illumination (compare to figure 1.27). An important result was the observation that the bilayer dielectric (SiO_2/teflon) exhibited substantially reduced hysteresis compared to the single layer (teflon) devices (figure 2.6). This effect is attributed to the motion of ions through the teflon dielectric. Because the hysteresis on the teflon-only devices was large the decision was made to use the bilayer devices for the electrowetting experiments in order to avoid having to control and account for this effect.

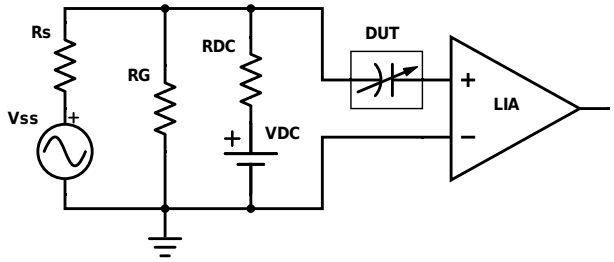

Figure 2.4: Circuit for CV characterization. MIS capacitor is labelled DUT (Device Under Test). The nominal resistivities of the components were $R_S = 50.0\,k\Omega$, $R_G = 100\,k\Omega$ and $R_{DC} = 10.0\,k\Omega$.

2.3.2.2 Doping Concentration

The conductivity of a doped semiconductor material is given by the formula $\sigma = eN\mu$. In this equation N is the doping concentration, the same parameter appearing in equation 2.8, e is the elementary charge and μ is the mobility, a known constant for electrons and holes in silicon. Hence N can be measured directly by measuring the resistivity. The resistivity of the sample used for the electrowetting experiments was

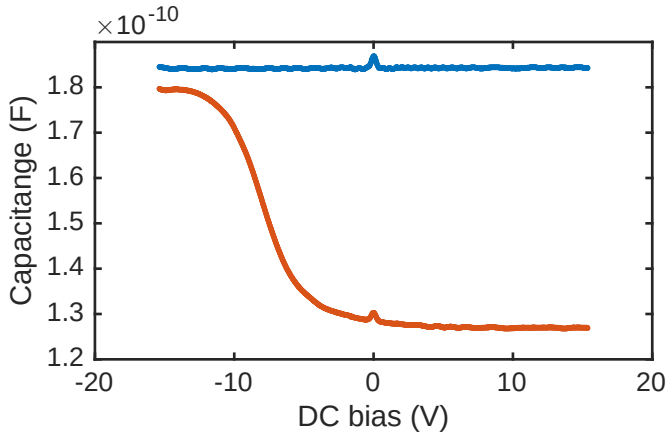

Figure 2.5: CV characteristics for Au/teflon/silicon devices in dark (red dots) and illuminated (blue dots) conditions. Ramp speed was 0.2 V/s, frequency was 1 kHz.

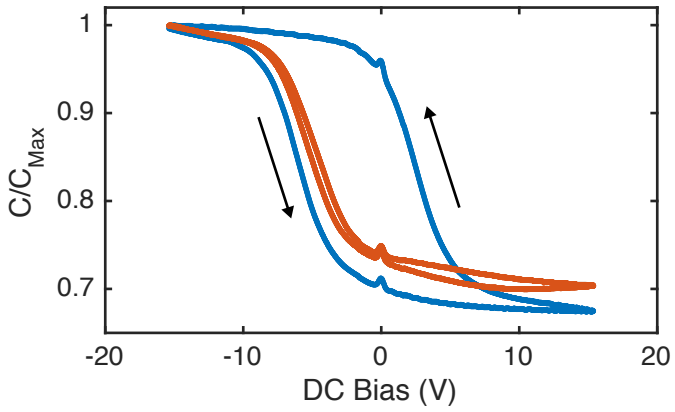

Figure 2.6: Capacitance versus voltage for a Au-Teflon-Si (blue, 0.2 V/s, 1 KHz) and a Au-Teflon-SiO_2-Si (red, 0.1 V/s, 1 KHz) capacitor.

measured using a four-point probe (Miller Design & Equipment FPP-5000). With this measurement, $\rho = 15.7$ Ω-cm, the hole concentration N_a was inferred to be $8.6 \times 10^{14}\,\mathrm{cm}^{-3}$.

2.3.2.3 Surface Tension

The surface tension of the electrolyte solution, γ_{lv} in equations 3.1 & 2.8, was measured using Wilhelmy's method. In this method an object with a well defined geometry, for instance a strip, is dipped into the solution (figure 2.8). The force of

surface tension on the object will be $F = p\gamma\cos\theta$, where p is the perimeter of the triple contact line, γ is the surface tension and θ is the contact angle. The force could be measured directly but in general the contact angle is not known a priori. In practice the object is pulled slowly out of the fluid and the force is measured continuously. As the object is pulled the force increases as the contact angle decreases, reaching a maximum just prior to breaking off when $\theta = 0$. If the contact angle is zero the force then becomes $F = p\gamma$, enabling a direct measurement of γ. The experiment is depicted in figure 2.7. A strip of filter paper was submerged in the electrolyte and the force on it was measured using a precision scale (Ohaus AS-313). The surface tension of the electrolyte was measured to be 72 mN/m.

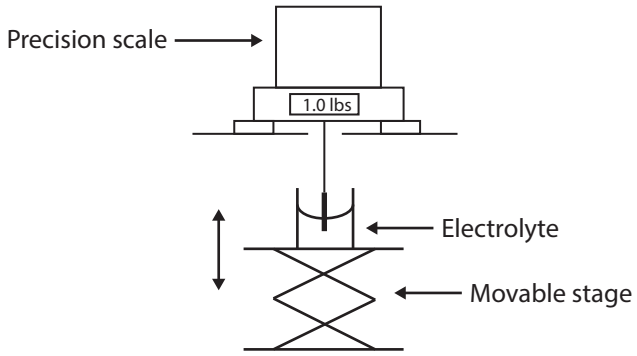

Figure 2.7: Setup for surface tension measurements.

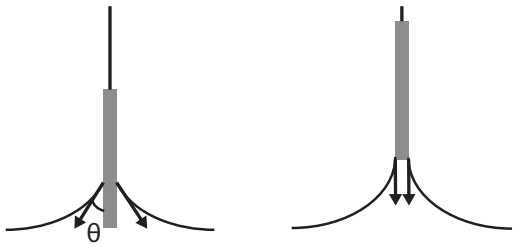

Figure 2.8: Closeup of strip. Arrows depict direction of surface tension force. At pinch-off the forces are parallel to the strip.

2.3.3 Electrowetting Experiments

The experiments were conducted using a 10 mM NaCl aqueous solution. The solution was prepared using deionized water and $\geq$ 98% NaCl (Sigma-Aldrich). A 5 μl drop was pipetted on to the teflon layer and a 0.14 mm steel wire was inserted into the apex of the drop (see Fig. 2.9). Voltages were applied across the wire and ohmic contacts with a source-measurement unit (Keithley 2400 SMU) and, following a short period (300 ms) for electrostatic and hydrodynamic equilibration, a digital image was recorded. The contact angle was extracted by processing this image. Current monitoring allowed observation of possible dielectric breakdown. Because the experiments are sensitive to above-bandgap light these were performed in a light-tight enclosure (figure 2.10). The drop was backlit with an infrared LED (λ = 1550 nm) and imaged with an infrared-sensitive camera (FLIR A2600sc). A typical image is shown in Fig. 2.9. To study the response of the drop to light a high power white LED (MCWHL5, Thorlabs) was used for illumination.

Electrowetting experiments were conducted in the three regimes of accumulation, deep-depletion and inversion. Our measurements in accumulation and inversion were made by increasing the magnitude of the applied bias in one volt steps starting at 15 volts because below this voltage we saw no change in the contact angle. In deep-depletion the measurements were taken at 5 volt steps to limit minority carrier generation during the experiment. To produce the inversion data sets, the LED was mounted in close proximity, aimed at the droplet and activated at full intensity (19 mW/cm^2) for 200 ms following application of the voltage.

2.3.4 Results & Analysis

A typical measurement of the photo-electrowetting effect is shown in fig. 2.11 (black circles). The data show a decrease in the contact angle following the application of a bias, followed by another decrease upon illuminating the drop. As expected from

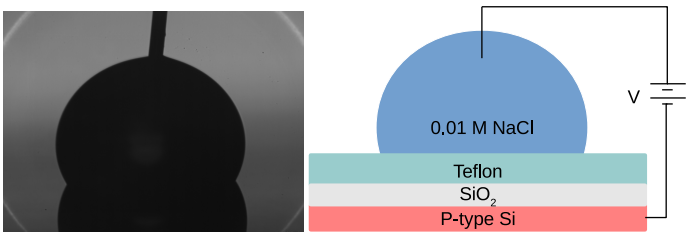

Figure 2.9: Electrowetting experiment. Left: image from infrared camera for contact angle measurement. Right: Device schematic (not to scale).

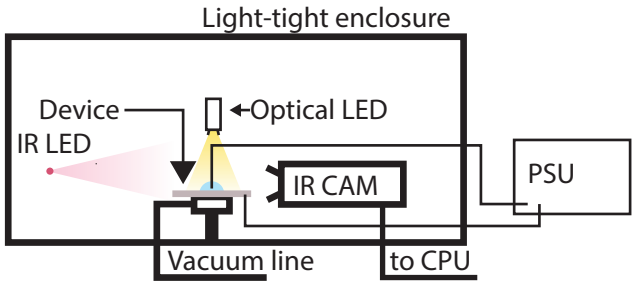

Figure 2.10: Setup for electrowetting experiments. A vacuum line leading to a set of grooves in the surface supporting the wafer holds the wafer in place.

our analysis, turning off the light source does not restore the contact angle to it's pre-illumination value. This is contrary to the findings reported in Arscott [2011].

The results of the experiments for the three electrowetting regimes are given in fig. 2.12. This data led to a couple of modifications of the model of equations 3.1 and 2.8. Between ±15 V there were no observable changes of the contact angle, indicating contact line pinning [de Gennes et al., 2004]. To account for this pinning threshold, the model was modified by replacing the equilibrium contact angle with the advancing contact angle θ_{adv} based on the following rationale. When the drop is first deposited on the surface, it spreads until the contact angle falls below the advancing contact angle. As the bias is increased the stress on the contact line increases until it exceeds the pinning threshold. Thus the advancing contact angle gives a measure of the pinning threshold, and its inclusion in the model accounts for this additional force on the contact line. The accumulation and inversion data sets (red and black

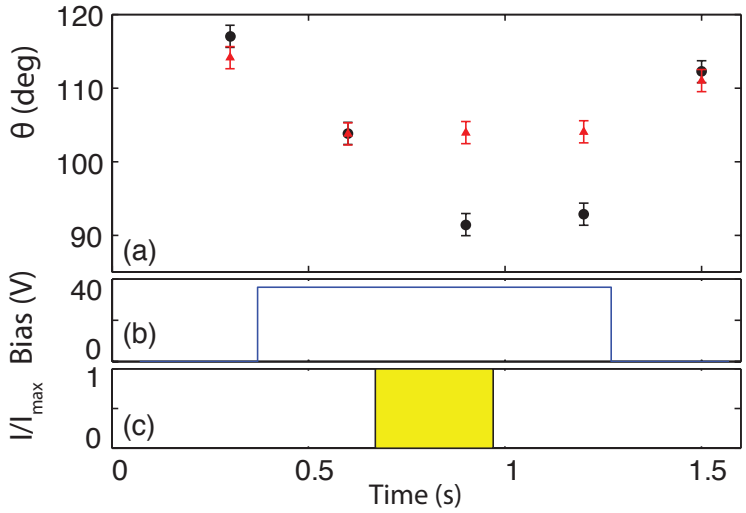

Figure 2.11: a) Contact angle versus time in an electrowetting experiment where the drop is illuminated (black circles) and not illuminated (red triangles). b) Applied bias vs time for both experiments. c) Illumination vs time for illuminated experiment normalized to full intensity (19 mW/cm^2). Note that turning off the illumination does not restore the pre-illumination value and that in the absence of illumination the second wetting transition does not occur. Error bars indicate reproducibility from run to run.

• in figure 2.12 respectively) are expected to follow the Young-Lippman equation as discussed previously, which is quadratic in the applied bias V. Nevertheless an asymmetry around zero volts in the form of an offset is apparent in these data sets. MIS capacitors are known to exhibit a shift in the flatband voltage [Sze and Ng, 2007] as a result of fixed oxide charges and work function differences between the silicon and the metal. Thus, a horizontal offset was introduced by replacing V with $(V - V_o)$ in the model to account for these effects.

With the modifications then new model is:

$$\cos\theta = \cos\theta_{adv} + \frac{c}{2\gamma_{\mathrm{lv}}}(V - V_o)^2 \tag{2.9}$$

$$\cos\theta = \cos\theta_{adv} + \frac{\lambda^2}{3\gamma_{\mathrm{lv}}c^3}\left[-1 - 3\tilde{V} + (1 + 2\tilde{V})^{3/2}\right] \tag{2.10}$$

Where equation 2.9 applies in accumulation and inversion and equation 2.10 applies

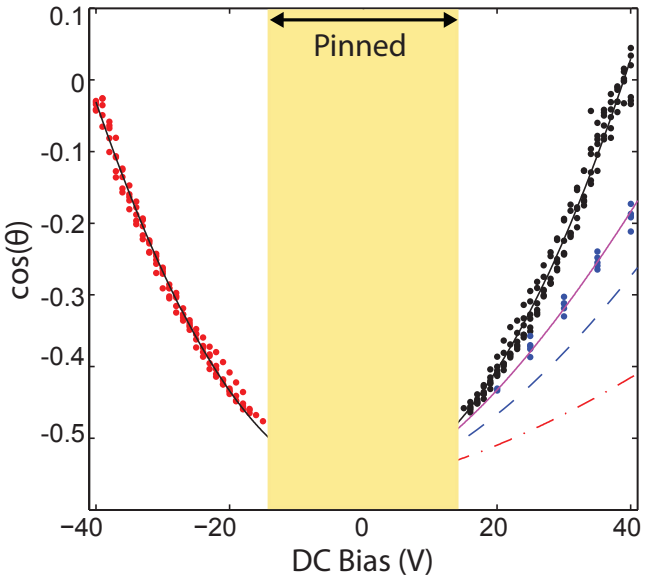

Figure 2.12: Electrowetting on p-type silicon for accumulation (red •), deep-depletion (blue •), and inversion (black •). The solid black line is a fit to the Young-Lippmann equation with a voltage offset. The dashed blue line is a plot of eq. 2.8 with the parameters obtained from fitting the accumulation and inversion data, and the magenta line is the same model with the addition of interface traps (eqn. 2.11). Red dot-dashed line depicts the earlier deep depletion model proposed by Arscott [2011]. No change in contact angle is observed in pinned region.

in deep-depletion, all for biases of magnitude larger than that of a threshold voltage. In equation 2.10, $\tilde{V} = c^2(V - V_o)/\lambda$.

The data were compared to the model by fitting the accumulation and inversion data sets to equation 2.9 and extracting the fitting parameters c, $\cos\theta_{adv}$ and the bias offset V_o. The fit yields $c = 5.0 \times 10^{-5}$ F/m^2, which is 7% lower than the value expected from thickness measurements, and a flatband offset of -1.1 V. Using these fit parameters and the measured values of the doping concentration and electrolyte surface tension the deep depletion prediction was computed from eq. 2.10. The result is plotted in fig. 2.12 as a dashed blue line; the model predicts a larger contact angle than observed.

Various effects were considered that might account for this discrepancy. The model relies on two approximations for the calculation of the electric field: the infinite plane

approximation and the depletion approximation for the charge distribution in the semiconductor. The actual charge distribution is finite in extent and the electric field exhibits so-called stray fields near the edges of the drop. Moreover in the depletion approximation the charge distribution ρ changes abruptly from complete depletion of carriers ($\rho = N$) to zero charge ($\rho = 0$). The actual charge distribution varies smoothly over a finite Debye length in the silicon. However, a finite element calculationsfor the free energy in depletion that took both these effects into account agrees with eq. 2.10 to within 0.5%. It was considered whether minority carrier generation through R-G center thermal recombination, or stray light leaking into our enclosure was prematurely inverting the charge distribution. It was also consider whether the inertia of the fluid was causing the contact line to overshoot the equilibrium value. In any of these cases, the discrepancy ought to exhibit a ramp rate dependence. However, ramp rates at 1 V/s and 5 V/s showed identical results.

Finally, interface traps were considered. Localized electronic states with energies in the forbidden gap are well known to appear at the Si/SiO_2 interface [Nicollian and Brews, 1982]. These states are found throughout the bandgap and are in electrical contact with the bulk. Unlike minorities carriers, interface states with energies close to the valence band respond quickly to changes in the surface potential. Note however that a transition from one interface trap to another is an unlikely event even when these two are close in energy given realistic values for trap densities at the Si/SiO_2 interface and their highly localized nature [Pierret and Neudeck, 1987]. Figure 2.13 depicts the interface traps and their proposed occupancy close to flatband and in deep-depletion. In eq. 2.4, where it had previously been assumed that $q = 0$ in deep depletion, the substitution is made $q = \sigma A$ where σ is the areal density of occupied traps. Combining eqns. 2.3, 2.5 & 2.6 and $(\partial q/\partial A)_Q = \sigma$ yields the prediction for

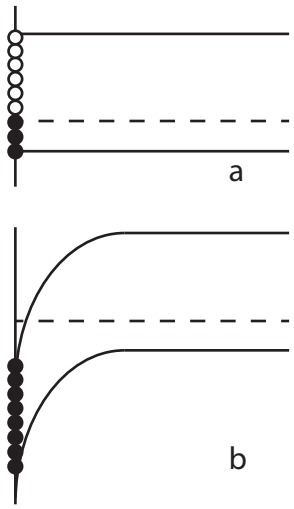

Figure 2.13: Band diagrams showing (a) trap occupancy close to $V_{flatband}$ and (b) in deep-depletion. Filled/unfilled circles depict occupied/unoccupied states. The dashed line represents the Fermi energy level in (a) and the quasi-Fermi level for holes in (b).

deep-depletion corrected for surface states:

$$\cos\theta = \cos\theta_{adv} + \frac{\lambda^2}{3\gamma_{\mathrm{lv}}c^3}\left[-1 + 3\tilde{\sigma} - \frac{3}{2}\tilde{\sigma}^2 + 3(\tilde{\sigma}-1)\tilde{V} + (1 + 2\tilde{V} - 2\tilde{\sigma})^{3/2}\right] \quad (2.11)$$

where again $\tilde{V} = c^2(V - V_o)/\lambda$ and $\tilde{\sigma} = c\sigma/\lambda$. A fit of the data to eq. 2.11 with σ as a free parameter and using the previously obtained values of c, $\cos\theta_{adv}$ and V_o gives a value of $\sigma = 1.8 \times 10^{11}\,\mathrm{cm}^{-2}$ that is well within the bounds for the fabrication process [Beadle et al., 1985]. Thus the discrepancy is attributed to interface traps.

2.4 Conclusion

In summary, the nature of the photoelectrowetting effect has been clarified and quantified. A light-induced transition has been observed to occur when the semiconductor is biased rapidly into inversion. An idealized model was introduced for the change in the contact angle as a function of the applied bias. The measurements showed a discrepancy between the data and the ideal model. With the introduction

of non-ideal effects due to contact line pinning, flat-band offset, and interface traps, the model accurately captures the physics of photoelectrowetting.

CHAPTER III

Droplet Motion with Photoelectrowetting

3.1 Introduction

Lab-on-a-chip devices are intended to perform standard laboratory functions with microliter fluid samples. There are many advantages to such precision technology: lower reagent usage, faster response times, lower capital equipment investment, compactness, portability and lower overall cost [Mark et al., 2010]. Moreover, the technology has the potential to usher in a new age of personalized medicine [Yager et al., 2006].

Transport of droplets between reaction sites is the most elementary task any lab-on-a-chip platform must perform. Multiple methods are now available to do this. Various passive wicking schemes have been discovered (*e.g.,* see Carrilho et al. [2009] for a recent variant). Techniques to transport droplets in devices molded from polydimethylsiloxane (PDMS) are widely employed [Duffy et al., 1998]. Yeo and Friend [2009] developed the surface wave acoustic technique (SAW) in which droplets are transported by waves on a piezoelectric substrate generated by interdigitated electrodes. Pollack et al. [2000] exploited the phenomenon of electrowetting-on-dielectric (EWOD) to transport droplets between electrodes with electrostatic forces. Other site-to-site transport techniques have been developed using localized heating [Darhuber et al., 2003] and optical control of electrowetting [Chiou et al., 2003].

Some of these techniques rely on a pre-fabricated transport network (channels in PDMS or on a wicking surface, etc.) that cannot be easily altered after fabrication, much less on the fly during an experiment. In contrast the EWOD-based approaches of Pollack and Chiou allow for instantaneous control of the direction of motion of the fluid. In the *optoelectrowetting* (OEW) technique developed by Chiou et al. [2008] they replaced the electrode grid used in earlier studies [Chiou et al., 2003] with a gridless photoconductive amorphous silicon layer configured in an EWOD stack. They demonstrated the ability to move a drop anywhere on a uniform substrate steered by a laser beam.

In this chapter we demonstrate another method of transport that also exploits a photo-triggered variant of EWOD. We show that a drop placed on single-crystal moderately doped silicon coated with an insulating film can be moved by shining light on the leading edge of the drop with typical speeds up to 1 cm/s, and sizes ranging from 2 µL to 20 µL (see Fig. 3.3). This technology has the advantage of using a featureless substrate, negating the need to employ complex photolithography techniques in fabrication as is required with traditional EWOD, SAW or PDMS devices. Because actuation is achieved by electrical means, as opposed to mechanical pumps, the platform is free of moving parts that reduce device lifetime and increase bulk, the latter being an important limitation on portability. Unlike devices where the fluid is confined to follow a predetermined path the drops can be moved in any direction at any time. The substrate can also be reused many times, in contrast to devices that actuate via wicking.

This approach differs from OEW in that it exploits a metastable charge distribution in moderately doped crystalline semiconductors. It shares the advantages of OEW but the device presented here is also easier to fabricate and is immune to degradation issues that arise with the use of amorphous silicon [Staebler and Wronski, 1977]. However due to the high mobility of charge carriers in crystal semiconductors

the approach presented here is ill suited for picoliter droplets, for which OEW devices may be substantially more effective.

3.2 Background

In electrowetting-on-dielectric [Berge, 1993] (Fig. 3.1a) a potential difference is applied across a droplet of electrolyte and a flat electrical conductor separated by an insulator. The droplet responds by spreading: the contact angle decreases and the liquid-solid interface expands. For small time-independent (DC) voltages the change is modeled well by the Young-Lippmann equation [Mugele et al., 2005]:

$$\cos\theta = \cos\theta_0 + \frac{c}{2\gamma}\phi^2 \tag{3.1}$$

where c is the per unit area capacitance of the dielectric, ϕ is the applied bias, γ is the surface tensions of the liquid-vapor interface and θ_0 is the contact angle at zero applied bias. By applying the effect asymmetrically through a pattern of electrodes as shown in Fig. 3.1b it is possible to induce bulk fluid motion [Pollack et al., 2000].

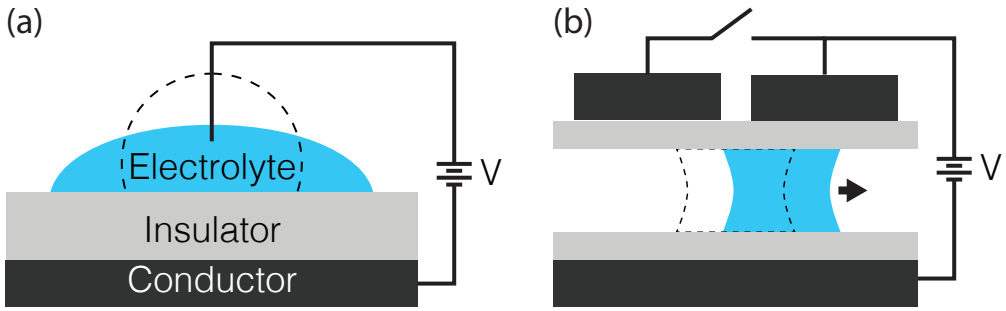

Figure 3.1: (a) A droplet of electrolyte undergoing a wetting transition in response to applied bias. (b) Droplet motion actuated in EWOD device. Dashed line outlines shape of drop prior to application of the potential.

Arscott [2011] discovered a new form of electrowetting when the conductor in the standard EWOD setup is replaced with a moderately doped crystalline silicon wafer.

As in standard EWOD the drop spreads in response to an imposed voltage bias. However, further spreading is induced by subsequent illumination of the drop with light. Arscott called this effect *photoelectrowetting* (PEW).

Palma and Deegan [2015] showed that photoelectrowetting is due to the equilibration of the charge distribution within the semiconductor from a long-lived non-equilibrium state (see Fig. 3.2). As noted by Arscott [2011], the liquid-insulator-semiconductor stack resembles the well-known MOS capacitor with its distinctive charge regimes: accumulation, deep-depletion and inversion [Sze and Ng, 2007]. A rapidly applied large DC bias (negative for n-type, positive for p-type) between the electrolyte and the semiconductor produces an initial spreading of the droplet and leaves the electronic state of the semiconductor in a metastable state, *deep-depletion*. The deeply-depleted state decays slowly towards the equilibrium state, *inversion*, by the thermal generation of electron-hole pairs at a rate proportional to the concentration of impurities; in typical semiconductor grade silicon this decay time is on the order of minutes for the large biases involved in electrowetting. Illumination, however, greatly reduces the equilibration time by photon mediated generation of electron-hole pairs. Thus, illuminating the droplet drives the silicon substrate into inversion, and due to that state's increased charge density the droplet spreads further. Since the transition from deep-depletion to inversion is thermodynamically downhill, the transition is irreversible and removing the light has no effect.

Based on these results we predicted that it would be possible to induce translation of a drop by a voltage-light sequence: (1) drive silicon into deep-depletion with a rapidly applied bias, (2) drive the charge distribution beneath one side of the drop into inversion thus creating an asymmetry in the charge distribution similar to that of a discrete electrode EWOD device, (3) reset the charge the distribution by zeroing the bias. Below we report the results of our experiments showing that this scenario does indeed result in drop translation and we construct a model to account for dependence

of the droplet speed on various experimental control parameters.

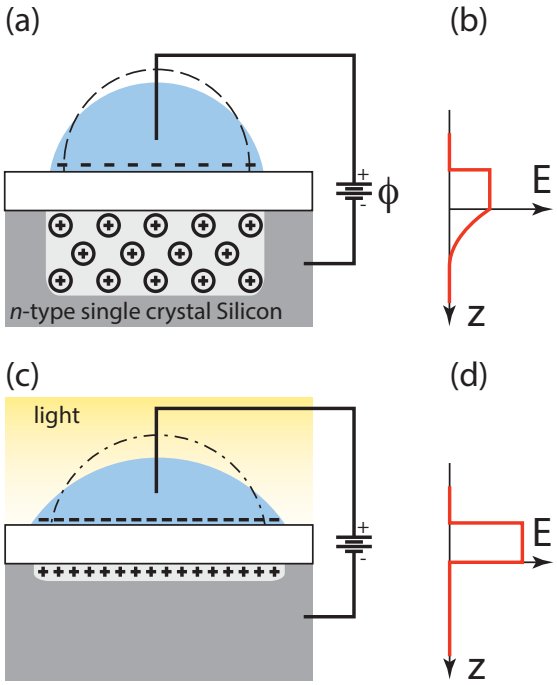

Figure 3.2: Photoelectrowetting effect for an n-type device. (a) Deep-depletion: applying a potential difference between the drop and the silicon induces spreading from initial state (dashed line). Charges in the silicon are immobile ionized dopants spread out over the so-called depletion layer. (c) Inversion: illumination generates mobile electron-hole pairs that replace the depletion region with an inversion layer, and cause further spreading. Holes here are depicted as + (b) & (d) Electric field in system as a function of depth for (a) & (c), respectively.

3.3 Experimental

3.3.1 Device Fabrication

We constructed photo-electrowetting devices on n-type (phosphorus) 4" silicon wafers (Silicon Valley Microelectronics) with nominal resistivity ($\rho = 1 - 10$ ohm-cm) using the following steps. First, we grew a 100 nm SiO_2 layer via dry oxidation at 1000° C for 125 minutes in an oxygen atmosphere containing trans 1,2-dichloroethylene (trans-LC), added to neutralize mobile ionic charges in the oxide,

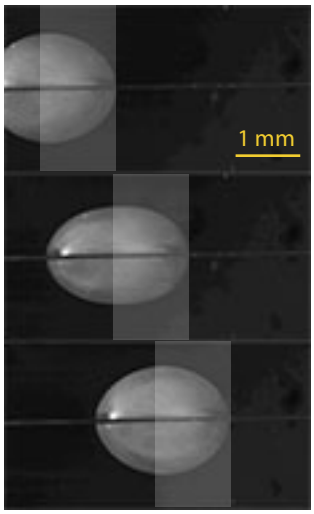

Figure 3.3: Sequential images of droplet motion actuated by photoelectrowetting. Pictures 1 sec apart. The laser line has been optically filtered out to prevent excessive glint; the lightened patches depict the position of the line. Microscopic particles were added to the fluid to enhance drop visibility.

followed by a 10 minute anneal in a nitrogen atmosphere. Next, ohmic contacts were formed by removing the oxide from the target areas with a diamond scribe, depositing a 1.5 μm aluminum layer on the now bare silicon via physical vapor deposition, and annealing at 500° C for 5 minutes in an argon atmosphere. Lastly, we deposited a teflon film on top of the oxide by spin coating a 2% (w/w) solution of Teflon AF1600 (Dupont) in FC-40 (Sigma-Aldrich) for 20 seconds at 500 rpm followed by 30 seconds at 1000 rpm. The film was then annealed in 1 atm N_2 for 15 minutes at 183° C followed by 15 minutes at 330° C. The resulting teflon film was 265 nm thick. The oxidation and ohmic contact deposition steps were performed in a class 100 cleanroom and the teflon deposition in a class 1000 cleanroom. The SiO_2 layer was added to create an insulator with high dielectric strength. Teflon was added on top of the SiO_2 to make the surface hydrophobic.. The capacitance per unit area of these insulating layers was 5.4×10^{-5} F/m^{-2}.

3.3.2 Experimental Setup

A volume 2 µL to 20 µL of electrolyte was pipetted directly on to the teflon coated surface so that the resulting drop bridged the gap between the surface and a stainless steel wire running parallel to the surface at a height of approximately 1 mm as shown in Fig. 3.4. Most experiments were conducted with 10 µL volumes that formed sessile drops with a contact angle of 62^o and a radius for the solid/liquid interface of $R = 2.2\,\text{mm}$. A potential difference was applied between the wire and silicon consisting of a sinusoidal part with amplitude ϕ_{AC} and frequency $0 < f \leq 100\,\text{kHz}$ superimposed on a DC bias ϕ_{DC} which for most experiments was $-7\,\text{V}$. The drop was illuminated continuously with a sheet of light produced by a 50 mW 660 nm laser (StockerYale Lasiris PureBeam) passed through a line generator that produced at typical working distances a line with 95% of the power spread within $\pm 0.6\,\text{mm}$ of the line center. The wire electrode was normal to the laser sheet, which was steered with a mirror mounted on a galvanometer (Thorlabs GVS002) in order to change its position.

An aqueous NaCl solution (1% w/w) with sodium dodecyl sulfate (SDS) (5 mM) was used for all experiments except those for different viscosities. The surfactant SDS was added to increase the magnitude of electrowetting (see Eq. 3.1). To vary the viscosity, solutions were prepared by adding acetic acid (1.0 M) and SDS (10 mM) to mixtures of water and glycerol in varying concentrations of the latter (0%, 29%, 40% and 48 % (w/w)).

3.4 Results

As shown in Fig. 3.3, we succeeded in actuating translational motion of the droplet. We characterized this phenomenon by measuring the maximum attainable speed of the droplet. The laser sheet was swept side to side with a fixed speed and in a direction parallel to the wire. At low speeds the droplet moved along with beam with

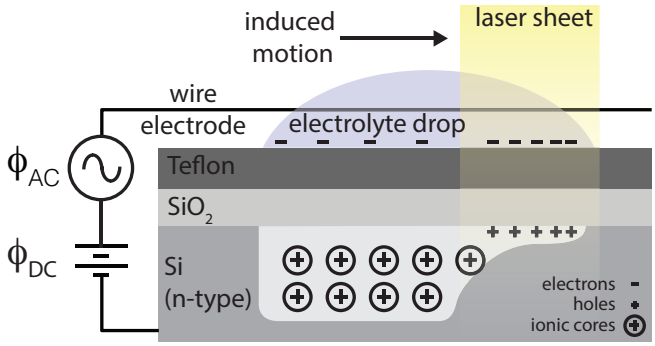

Figure 3.4: Experimental setup for droplet motion with photo-electrowetting. The substrate consists of silicon wafer topped with an oxide and a teflon film. A straight stainless steel wire runs parallel to the substrate approximately 1 mm from the surface. A drop of electrolyte bridges the gap between the wire and the surface. A voltage is applied between the wire and the substrate. When the bias is negative the semiconductor is in inversion under the beam and depletion on the dark side. Because the wettability is higher on the inverted side the drop edge moves towards the light. Not to scale.

no lag, with the beam centered at the center of the drop. As the speed was ramped up the center of the drop began to lag behind the center of the beam. At a certain speed that we call the maximum speed the drop could no longer keep up. We measured this maximum speed as a function of the frequency of the applied bias. These data are shown in Fig. 3.5.

Further experiments were conducted to look at the dependence of the maximum speed on ϕ_{AC} (Fig. 3.6), laser intensity (Fig. 3.7), droplet size (Fig. 3.8), and viscosity (Fig. 3.9). These data show that the speed increases monotonically with increasing drop size, decreasing viscosity and increasing driving voltage. The maximum speed also increases with illumination intensity up to a value around 25 mW/cm^2 and thereafter saturates.

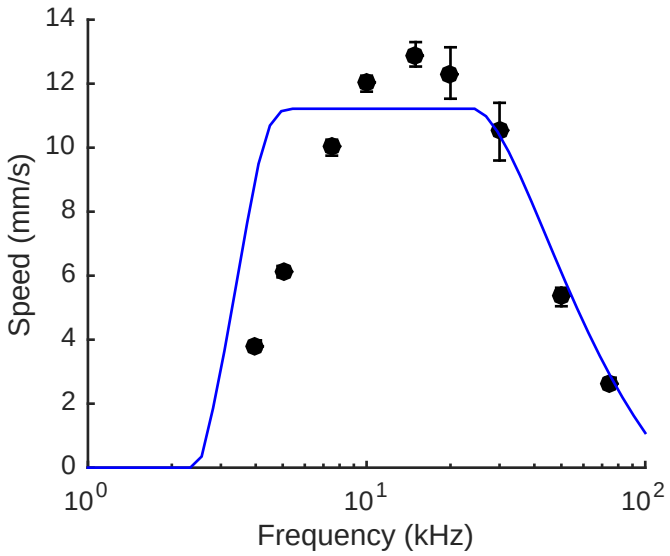

Figure 3.5: Max speed vs frequency of applied bias. Blue line corresponds to theoretical prediction as presented in discussion section.

3.5 Discussion

The mechanism driving drop translation is illustrated in Fig. 3.2 and Fig. 3.4 for n-type devices.[1] When the bias is negative the silicon below the drop becomes deeply-depleted, *i.e.,* a metastable layer of ionized donors forms that stretches deep into the silicon. When exposed to above-bandgap illumination the charge configuration is rapidly driven into equilibrium. Photogenerated electron-hole pairs are created, the electrons recombine with and neutralize the ionized donors, and the holes migrate to oxide-silicon interface, creating an inversion layer. The increased charge density of inversion causes the drop to spread further.

In our experiments we apply an AC bias and illuminate one side of the droplet continuously. On the dark side of the drop the charge configuration varies between accumulation when the voltage is positive and deep depletion when voltage is negative, while on the illuminated side the configuration varies between accumulation and inversion. The asymmetry in the charge state gives rise to an instantaneous force on

[1]The same mechanisms apply to p-type devices but all the signs are reversed.

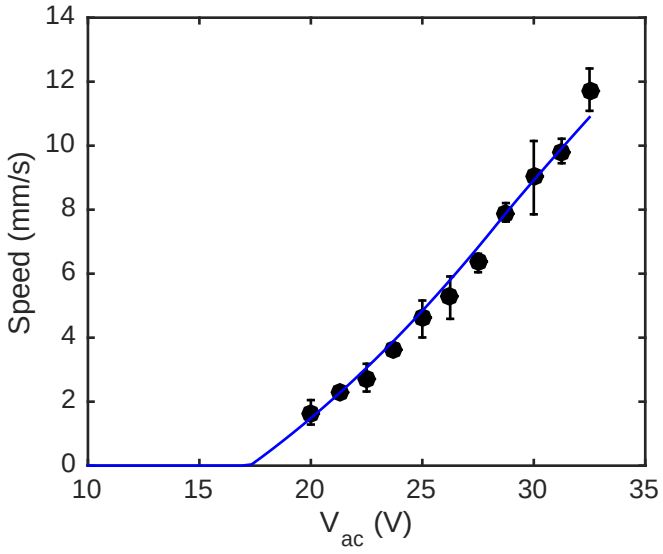

Figure 3.6: Max speed vs magnitude of applied bias. Blue line is theoretical prediction.

the droplet. This force occurs only when the bias is negative; for a positive bias the semiconductor is in accumulation everywhere, the asymmetry is lost, and therefore the force vanishes.

The data in Fig. 3.5 show that there is an optimal cycling frequency for producing droplet translation. The measurements discussed below show that the optimal frequency lies in a window that ends on the low frequency side because of minority carrier transport on long time scales and on the high frequency side because of low number of photons on short time scales. These effects are explained next.

At high frequencies the electrowetting force is limited by the generation rate of photogenerated electron-hole pairs. For the lit side to be inverted there must be enough incident photons to generate the necessary surface charge density $\Sigma = c\phi$ during the half cycle when the silicon is reverse biased. Here c is the capacitance per unit area of the insulating films, and ϕ is the voltage bias. Thus, the silicon is fully inverted for a given intensity I (power per unit area) when $c\frac{d\phi}{dt} < qI/\varepsilon$ or $f < f_c$ where q is the electron charge, ε is the energy of the photons, and $f_c = \frac{qI}{2\pi\varepsilon c\phi}$ is a

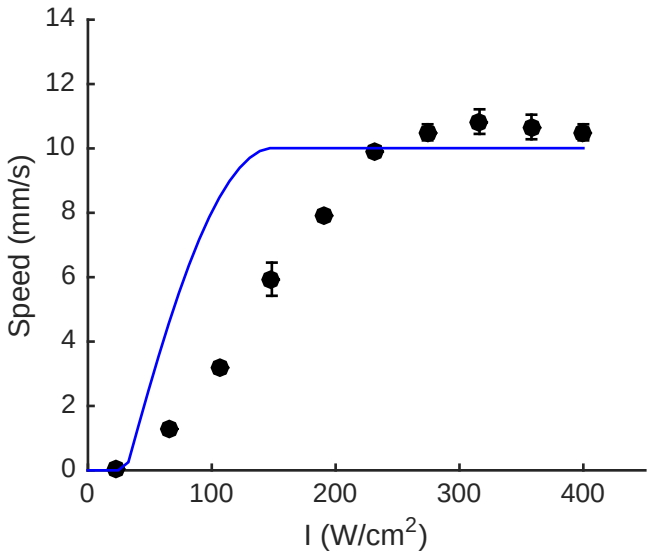

Figure 3.7: Max speed vs intensity of illumination. Blue line is theoretical prediction.

frequency threshold.

We independently verified this assertion by measuring as a function of frequency the contact angle of a drop with and without light. We used the same setup as in the motion experiments, except the laser sheet was applied parallel to the wire, such that both edges were illuminated. These data (Fig. 3.10) show that the dark contact angle is a constant 68° C up to the highest measured frequency. This constancy shows up to 100 kHz the conductivity of the electrolyte and the resistivity of the semiconductor make a negligible contribution to the total impedance. Were this not the case the potential drop across the insulator layer, which is the primary determinant of the change in the contact angle, would decrease in this frequency range and the contact angle would change. The lit contact angle is also a constant 57° C up to around 25 kHz, but thereafter rises with frequency until around 100 kHz where it approaches the dark value. The increase of the lit contact angle at frequency close to $f_c = 15$ kHz indicates that at high frequencies not enough minority carriers are being produced by the laser to fully create the inversion layer.

At low frequencies charge transport softens the horizontal gradient of the charge

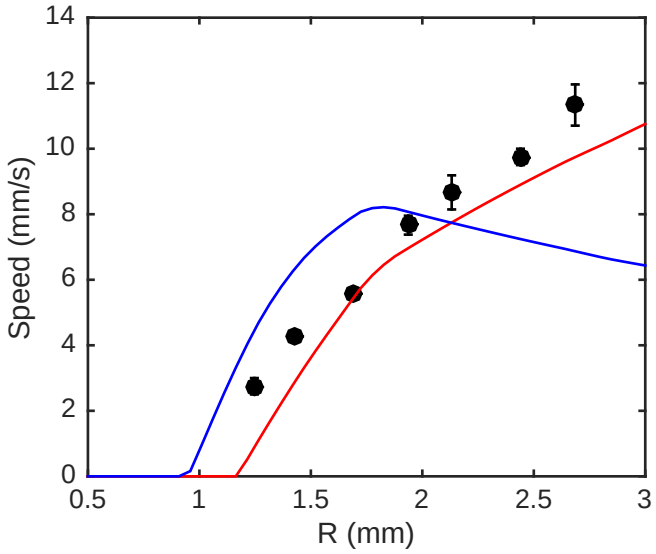

Figure 3.8: Max speed vs radius of solid/liquid insulator. Blue line is theoretical prediction. Red line is theoretical prediction with pinning and drag forces unscaled as the radius changes.

distribution diminishing the force. The timescale for the minorities carriers to cross the drop τ sets an upper bound for the period over which the drop experiences a force. For frequencies $f\tau \ll 1$ the drop experiences no forcing during most of a cycle, and thus the average force increases with increasing f. At $f\tau \gg 1$ the migration of minorities carriers is irrelevant since the bias is reversed before the carriers can move a significant distance.

We determined τ empirically by making a metal-insulator-silicon (MIS) capacitor and measuring the equilibration time of this device in response to localized illumination. Circular, semitransparent [Axelevitch et al., 2012] gold electrodes were deposited on the upper teflon surface of a wafer prepared as described in the experimental section. The electrodes were 205 Å thick with a radius of 1.0 mm chosen to approximate the area of the solid/liquid interface in the drop motion experiments. Following application of a DC potential between the electrode and the ohmic contact laser light was shone on the gold electrode and the current was measured with an oscilloscope from

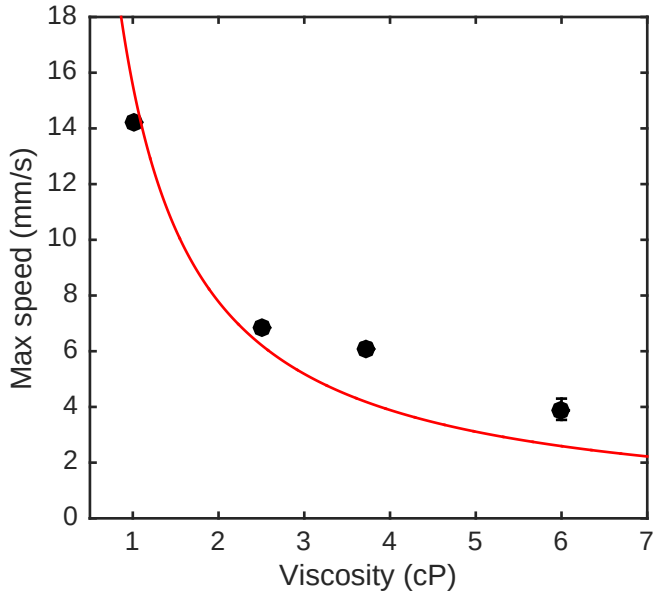

Figure 3.9: Maximum drop speed versus viscosity at $f = 20\,\mathrm{kHz}$, $\phi_{AC} = 27.5\,\mathrm{V}$, $\phi_{DC} = -7\,\mathrm{V}$, and $I = 40\,\mathrm{mW/cm^2}$ for 10 μL droplet of an acetic acid (1.0 M) solution in water with a surfactant (10 mM SDS) and varying glycerol concentrations. Line corresponds to a $1/\eta$ fit.

the potential across a small resistor in series with the MOS capacitor. The half-width of the laser line was 0.71 mm and thus smaller than the electrode. The intensity of the laser line was set to $500\,\mathrm{mW/cm^2}$, chosen such that the intensity of radiation incident on the semiconductor, corrected for absorption by gold layer, matched the intensities in the experiments with the drops.

Light induces a current as the capacitance increases during the transition from deep-depletion to inversion. Measuring the time-scale for this current to vanish yields a measure of τ. Two typical measurements for different positions of the laser beam are shown in Fig. 3.11. The blue and red curves correspond to a measurements with the laser line positioned near the edge and at the center of the disc, respectively, and the longer relaxation time of the blue reflects the greater distance the photogenerated minorities carriers must travel. Additional measurements for different distances of the laser line to the edge of the disc are shown in Fig. 3.12. These data give an empirical relationship between τ and the position of the laser.

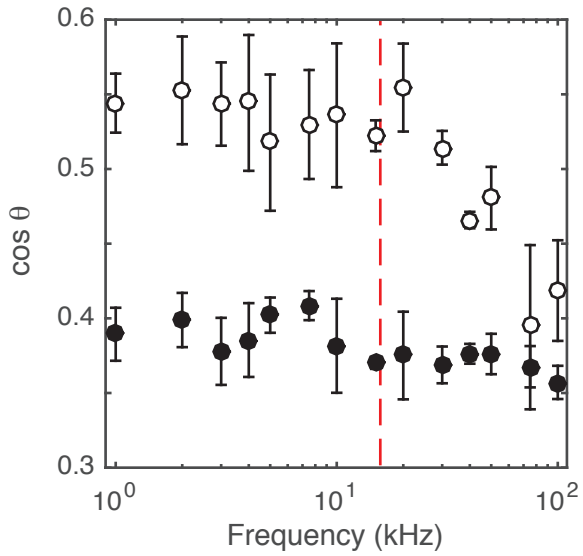

Figure 3.10: Cosine of the advancing contact angle versus frequency of applied bias with (∘) and without (•) illumination for $\phi_{AC} = 32.5\,\mathrm{V}$, $\phi_{DC} = -7\,\mathrm{V}$, and $I = 40\,\mathrm{mW/cm^2}$. The dashed red line shows the theoretical frequency threshold f_c. Droplets were 10 µL of a solution of NaCl (1% w/w) with a surfactant (5 mM SDS).

In summary, there is a frequency window $\tau^{-1} < f < f_c$ where the force generated by photoelectrowetting is strongest. These effects are summarized graphically in Fig. 3.13. In order to generate a prediction for the speed of the droplet these effects can be combined with an electrostatic computation of the force on the drop. In the proposed model the instantaneous force F is a function of the beam position within the drop x_c, it's intensity as well as the frequency and magnitude of the applied bias. The Maxwell stress and the resulting force can be obtained from the electric field configurations derived in Palma and Deegan [2015], as will be detailed in the next section. Because the interest is in the maximum speed, the instantaneous force is maximized with respect to x_c. The force varies as the potential swings between positive and negative biases. Hence the force is averaged over a cycle:

$$\bar{F} = f \int_0^{t_e} \mathrm{d}t \; F(x_c, I, f, \phi(t)) \tag{3.2}$$

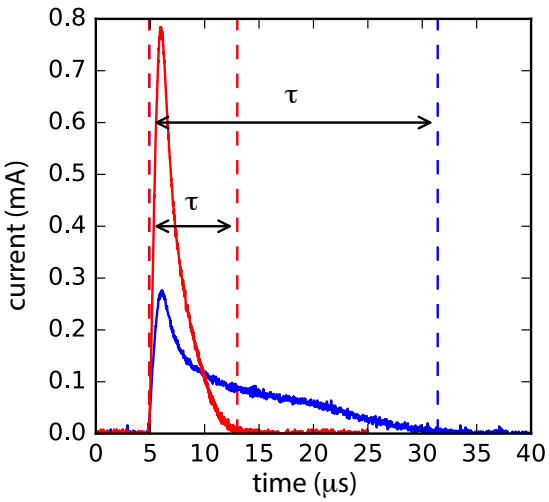

Figure 3.11: Current versus time following illumination of a gold-telfon-oxide-silicon capacitor with a laser line generator striking the gold electrode close to the edge (blue) and in the center (red). The laser locally generates electron-hole pairs. A current into the MOS capacitor is induced because of the increased net capacitance of the inversion state. The current stops when the minority carriers generated by the beam cover the entire surface with an inversion layer. Here τ denotes the time needed in each case for the entire capacitor to be inverted. The peak intensity of the laser line was 500 mW/cm^2. For comparison the RC time constant for accumulation biases is expected to be no higher than 0.3 µs.

The upper limit of the integral t_e is set by which ever is smaller of half period $((2f)^{-1})$ and the time for the minority carriers to cross the drop (τ). The latter approximates the force nullifying effect when minorities carriers diffuse or drift into the unlit region.

The blue curves in figures 3.5 - 3.8 depict the prediction of this model. In order to relate the speed of the droplet u to the force $\bar{F}$ a force balance was established $F_d = \bar{F} - F_p$, where F_d is the hydrodynamic drag force and F_p is the force from contact line pinning. The simplest approximation for the drag force $F_P = \xi^{-1}u$ is chosen, which yields $u = \xi(\bar{F} - F_p)$. The values of ξ and F_p are extracted as fitting parameters from the speed versus AC magnituce data and used as fixed values when computing the other curves. The best fit to the data yields $\xi = 0.69 \times 10^2$ mm/s/µN and $F_p = 6$ µN. These values are in line with literature values. For example Le Grand

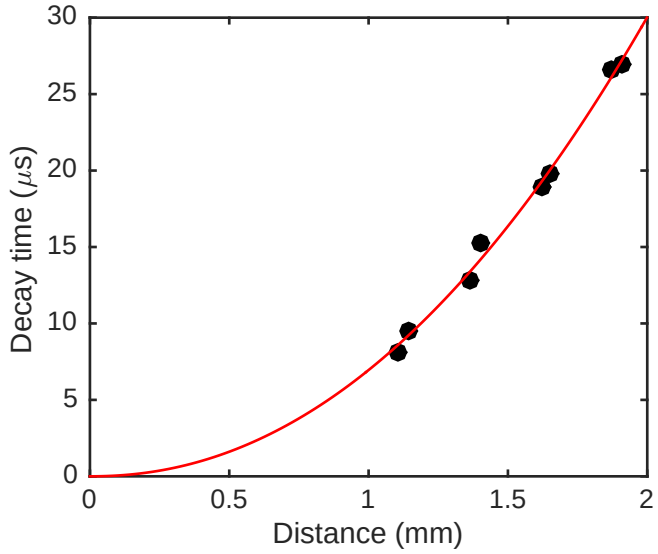

Figure 3.12: Transit time τ versus distance x determined by the decay time of the current following illumination (see Fig. 3.11). The line is a power law fit that yields an exponent of 2.1 ± 0.2 and a prefactor of $6.9 \pm 0.7\,\mu\text{s/mm}^{2.1}$.

et al. [2005] found for 6 µL droplets of 10 cP silicone oil running down an inclined plane $\xi = 0.37 \times 10^2\,\text{mm/s/µN}$ and $F_p = 6.2\,\text{µN}$.

The speed dependence on the volume of the droplet (figure 3.8) is not qualitative correct. Based on the theory of contact line dynamics [De Gennes, 1985] we expect $\xi \sim R$ and $F_p \sim R$. Applying these scalings gives the theoretical curves in blue in figures 3.5 - 3.8. The model prediction for the radius dependence exhibits a maximum that disappears when no scaling is used (red curve). There are at least two reasons to suspect the force-speed relation: the Reynolds number is 30[2] and thus not low, and we observe changes in the aspect ratio of the drop in motion (see figure 3.3) to the drop in motion that change the length of the contact line. While the predictions is worst in the volume dependence curves, it is likely that the agreement of other quantities with the predictions would also benefit from a better force-speed relation. Given the difficulties found in the low Reynolds number limit [Bonn et al., 2009], this avenue is not pursued.

[2]For $v = 15\,\text{mm/s}$, density $1\,\text{g/cm}^3$, $\eta = 1$ cP, and a length scale of 2 mm

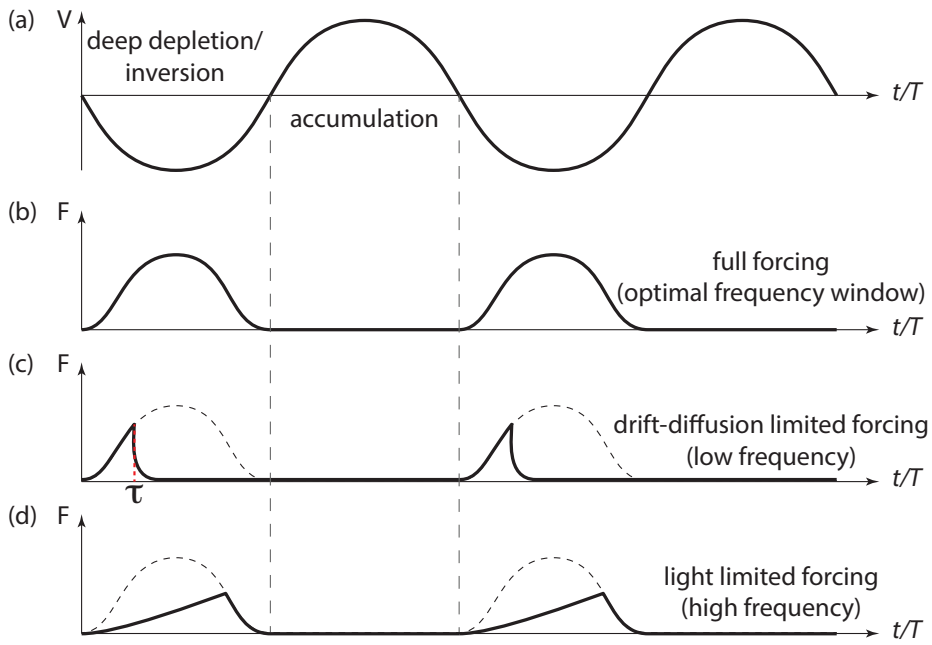

Figure 3.13: Photoelectrowetting force as a function of time for a sinusoidal voltage applied to an n-type device. (a) For negative voltages the device is partially or fully inverted when illuminated and in deep depletion when dark; for positive voltages the device is in accumulation regardless of the illumination level. The force is present only for negative voltages as this is the only situation in which light can break the symmetry. During the negative part of the cycle, the force is due to the difference in the charge distribution beneath the drop on either side. (b) For frequencies in the optimal frequency window, the force is active throughout the negative bias part of the cycle. (c) For low frequencies the duration of the forcing is abbreviated by drift and diffusion of minority carriers across the drop that weaken the differences in the charge charge distribution. (d) For high frequencies the number of photogenerated minorities carriers is insufficient to establish the larger difference in the charge distribution that would present at lower frequencies.

3.6 Computation of force

The drop is divided into dark and lit regions as shown in Fig. 3.14. The force on the drop in the direction of the light gradient (y) is opposite to the force on the dielectric media below the drop, both the insulating film and the silicon:

$$F = -\oint_S \sigma_{yy} n_y \mathrm{d}S \tag{3.3}$$

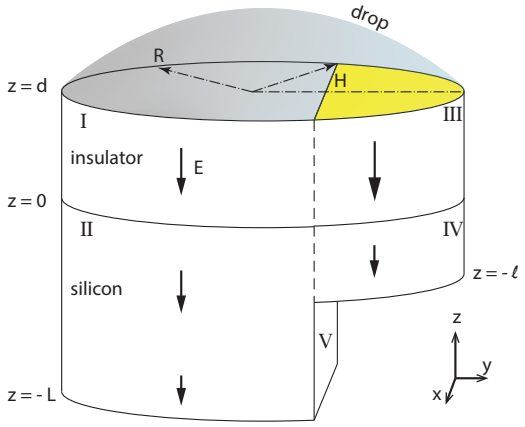

Figure 3.14: Geometry for computation of photoelectrowetting force. Arrows denote the electric field. The illuminated portion of the drop is depicted in yellow.

where σ_{yy} is the only contributing component of the Maxwell stress, n_y is y component of the surface normal, and S is the surface completely enclosing the dielectric and the silicon. We neglect fringe fields and assume the electric field is entirely in the z direction. The only surfaces with non-vanishing contributions are labeled I-V in Fig. 3.14 and yield:

$$F = 2H\left[\int_0^d \sigma_{yy}^I \mathrm{d}z - \int_0^d \sigma_{yy}^{III}\mathrm{d}z + \int_{-L}^0 \sigma_{yy}^{II}\mathrm{d}z - \int_{-\ell}^0 \sigma_{yy}^{IV}\mathrm{d}z - \int_{-L}^{-\ell} \sigma_{yy}^{V}\mathrm{d}z\right] \tag{3.4}$$

where H is the half width of the lit area defined in Fig. 3.14. The electric fields are constant in the insulator film and linear in the silicon (see Palma and Deegan [2015]):

$$E^I = E_1 \tag{3.5}$$

$$E^{II} = E_2(1 + z/L) \tag{3.6}$$

$$E^{III} = E_3 \tag{3.7}$$

$$E^{IV} = E_4(1 + z/\ell) \tag{3.8}$$

$$E^{V} = E_2(1 + z/L) \tag{3.9}$$

Continuity of the electric displacement field at the silicon-dielectric boundary and Gauss's law requires:

$$\epsilon_d E_1 = \epsilon_s E_2 = \Sigma_D \tag{3.10}$$

$$\epsilon_d E_3 = \epsilon_s E_4 = \Sigma_L \tag{3.11}$$

Here $\Sigma_{L,D}$ are the total charges per unit area in the lit and dark parts of the drop at the liquid-insulator interface.

Using $\sigma_{yy} = -\frac{1}{2}\epsilon E^2$,

$$F(t, x_c) = H\left[\Sigma_L^2 \left\{\frac{d}{\epsilon_d} + \frac{\ell}{3\epsilon_s}\right\} - \Sigma_D^2 \left\{\frac{d}{\epsilon_d} + \frac{\ell}{\epsilon_s}\left(1 - \frac{\ell}{L} + \frac{\ell^2}{3L^2}\right)\right\}\right] \tag{3.12}$$

where the time and beam position dependence are made explicit.

The relation between the surface charges and the voltage are also presented in Palma and Deegan [2015]:

$$\phi = \frac{\Sigma_L}{c} + \frac{(\Sigma_L - \sigma - \sigma_s)^2}{2\lambda} \tag{3.13}$$

$$= \frac{\Sigma_D}{c} + \frac{(\Sigma_D - \sigma_s)^2}{2\lambda} \tag{3.14}$$

where σ is the minority carrier charge per unit area, σ_s is the surface state charge per unit area, and $\lambda = e\epsilon_s N$ and N is the number of donors per unit volume. The difference between Eq. 3.13 and 3.14 is the absence of a minority charge term in the latter, reflecting the absence of minority carriers on the dark side. The values of ℓ and L follow from the zero net charge condition:

$$\Sigma_L = \sigma + \sigma_s + eN\ell \tag{3.15}$$

$$\Sigma_D = \sigma_s + eNL \tag{3.16}$$

This completes the specification of the model. As ϕ varies with time, so does F. We find this variation by the following procedure starting from $\phi = 0$, $\Sigma_{L,D}$=0 at $t = 0$:

1. $\phi(t) = \phi_{DC} + \phi_{AC} \sin 2\pi f(t - t_0)$ where t_0 is selected so that $\phi(0) = 0$.

2. The surface states charge rapidly and so σ_s follows $\Sigma_{L,D}$ until the surface states saturate at some time t_s determined by the saturation value eG where e is the charge of the electron and G is the number of surface states per unit area. During this phase,

$$\Sigma_{L,D} = c\phi \tag{3.17}$$

   since the second term in Eq. 3.13 & 3.14 vanishes, $\ell = 0$, and $L = 0$, and so $F = 0$.

3. Once the surface states are fully charged σ, ℓ, or L can begin to grow.

   - For the lit area σ will follow $\Sigma_L - \sigma_s$ if there is enough light to generate the necessary minority carriers, and if not, it will be limited to the number of photogenerated electrons. For sufficient light $\ell = 0$, $\Sigma_L = c\phi$; for insufficient light $\sigma = eI(t - t_s)/\varepsilon$, Σ_L is found by solving Eq. 3.13, and ℓ is given by Eq. 3.15.
   - For the dark area Σ_D is found by solving Eq. 3.14, and L is given by Eq. 3.16.

This algorithm gives the appropriate force when the drop is uniformly lit over a fraction of the area as shown in Fig. 3.14. However, in our experiments the light sheet illuminates the drop with a gaussian profile with a 1.2 mm width, defined as containing 95% of the power. We approximate this condition as a strip of width $w = 1.2$ mm with constant intensity and the total power equal to that of the beam. Depending on the position of the laser the strip may lie partially inside the drop in

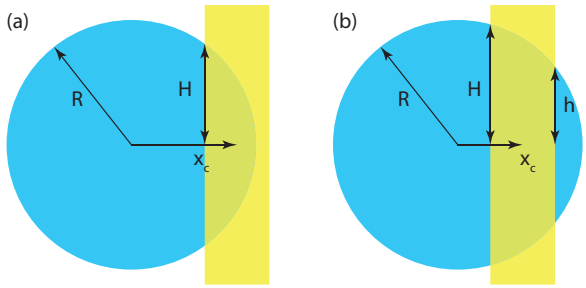

Figure 3.15: Geometry for different centers of the laser sheet.

which case Eq. 3.12 is the appropriate form of the force, or it may lie entirely within the drop, flanked by two dark zones in which case a similar calculation shows that Eq. 3.12 with $H - h$ instead of H is the the appropriate force.

The force is then averaged over the cycle as discussed in the last section. The resulting force depends on the position of the beam which enters overtly through H and also through the value of τ, which varies as the square of the distance between the beam edge and the far edge of the drop. Since we want to know the maximum speed, we select the beam position that maximizes the force.

3.7 Comparison with optoelectrowetting

Chiou *et al.* used light to actuate droplet motion on an amorphous silicon substrate. They observed fluid spreading in response to the instantaneous application of an AC bias and above-bandgap illumination that they termed *optoelectrowetting* and model this phenomenon with Eq. 3.1 in which ϕ is replaced by the root-mean-squared voltage across the insulator layer. In their model light decreases the impedance of the photo-conductive layer, increasing the root-mean-squared voltage across the insulator. They achieve droplet motion by confining the light to one side of the droplet.

Optoelectrowetting is a different phenomenon from photoelectrowetting. The most obvious difference is the absence of a deep depletion layer in optoelectrowetting. Thus in contrast to photoelectrowetting which is inherently a non-equilibrium phenomenon,

optoelectrowetting is an equilibrium phenomenon and it is modeled using linear response. The difference is most notable in the low and high frequency limits. Optoelectrowetting in these limits vanishes because the impedance difference between the lit and dark regions is dominated by components unaffected by light. Photoelectrowetting also vanishes in these limits but due to different reasons. In the low frequency limit the non-equilibrium state relaxes and in the high frequency limit there is not enough light. Thus, increasing the light power can extend frequency response for photoelectrowetting, but not for OEW.

Another key difference stems from the low mobility of carriers in amorphous silicon compared to crystal silicon, a difference of five orders of magnitude [Sze and Ng, 2007, Moore, 1977] for electrons. This means that unlike photoelectrowetting, the optoelectrowetting effect is well confined to the illuminated regions of the droplet in the range of frequencies explored in this work. A consequence of this confinement is that optoelectrowetting actuation is easier to apply to smaller droplets [Pei et al., 2010]. With photoelectrowetting, the time necessary for minority carriers to reach the trailing end of the droplet decreases with smaller droplets, hence decreasing the actuation force. This can be mitigated with the use of higher frequencies but this in turn implies increased electrolyte concentrations, higher laser intensities and/or larger applied biases.

As a practical device, photoelectrowetting has advantages in durability and manufacturability. Amorphous silicon devices have to contend with the Staebler-Wronski effect [Staebler and Wronski, 1977], that decreases the dark conductivity and photoconductivity significantly after prolonged exposure to intense light. This degradation will eventually produce patches in which OEW is weak. The device presented here is also easier to fabricate, especially for a researcher without on-site access to microelectronic fabrication facilities. As noted by Whitesides [Whitesides, 2006], ease of fabrication has been a deciding factor in the growing popularity of PDMS microflu-

idic devices. Optoelectrowetting devices presented thus far require sophisticated clean room techinques: plasma-enhanced chemical vapor deposition equipment to deposit the amorphous silicon and atomic layer deposition [Pei et al., 2010] equipment for the insulator. In contrast, a photoelectrowetting device can be constructed from commercially-available pre-oxidized silicon wafers, and the the teflon can be obtained by simpler spin coating or even dip coating.

3.8 Conclusions

In this chapter droplet actuation via exploitation of the photoelectrowetting effect has been demonstrated. The dependence of the speed of the droplet with several experimental parameters has been explored and modeled, including the potential, laser intensity, fluid viscosity and droplet size. The origin of the frequency band appropriate for photoelectrowetting actuation has been explained. A comprehensive comparison to OEW actuation has been presented with a discussion of the relative strengths and weaknesses of each. An easy to construct platform for droplet manipulation in microfluidic applications has been presented.

CHAPTER IV

Minority Carrier Dynamics in Depletion Regions

4.1 Introduction & Background

As showed in the previous chapter, the migration of carriers from the illuminated to the non-illuminated regions of the depletion region has significant consequences for the droplet actuation scheme presented in this thesis. It sets the lower bound for the bias frequency necessary for actuation and it dictates the smallest droplet size that can be actuated for a given frequency. In addition, the motion of charge carriers in depletion regions is a technologically important problem that arises in CCDs and field effect transistors. In this chapter the problem of minority carrier migration in depletion regions is studied using finite element simulations. I will show that the distribution of charge carriers exhibits self-similarity in space and time. This fortuitous development allows small scale calculations to be scaled up. These self-similar dynamics can thus be used to construct a scaling model that captures the physics of photoelectrowetting actuation.

Electrowetting [Mugele et al., 2005] refers to the spreading of a liquid that occurs when an electric potential difference is applied between an electrolyte droplet and a conductor separated by an insulator (figure 4.1a). By inducing the effect asymmetrically [Pollack et al., 2000] with discrete electrodes it is possible to translate droplets (figure 4.1b).

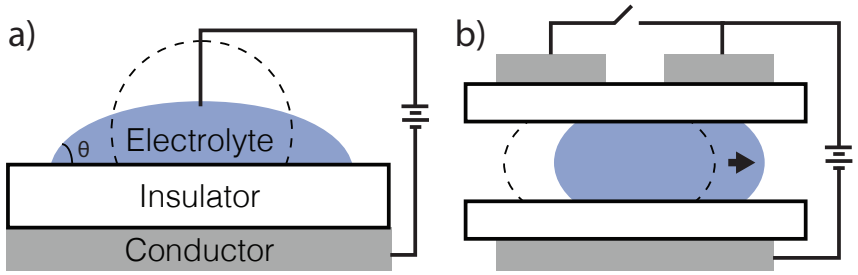

Figure 4.1: a) The electrowetting effect. b) Droplet motion induced by asymmetrical application of the electrowetting effect. Dashed lines in both figures delineate fluid prior to application of the electrical bias.

In photoelectrowetting [Arscott, 2011] (PEW) the conductor is replaced by a moderately doped semiconductor (figure 4.2). As noted by Arscott the liquid-insulator-semiconductor stack resembles the well known metal-oxide-semiconductor (MOS) capacitor with its distinctive capacitance regimes: accumulation, depletion and inversion [Sze and Ng, 2007]. If the semiconductor is an n-type wafer, rapid application of a large negative bias between the fluid and the semiconductor leaves it in deep-depletion. Charge is injected into the fluid and a wetting transition takes place: the fluid spreads on the substrate and the contact angle is reduced. Upon illumination with above-bandgap light, or light with photons of energy greater than the bandgap, minority carriers are rapidly generated and the semiconductor equilibriates into inversion. The inversion state has a greater net capacitance hence more charge is injected into the droplet and a second wetting transition takes place.

In chapter III we presented the technique by which the photoelectrowetting effect can be exploited to achieve translational actuation. By repeatedly applying photoelectrowetting to one side of the droplet (figure 4.3) it is possibly to induce droplet motion. The setup mimics the asymmetric application of electrowetting with discrete metal electrodes used by Pollack et al. [2000], but with the light beam effectively creating a virtual electrode.

As noted previously, photoelectrowetting is due to the creation of minority carriers

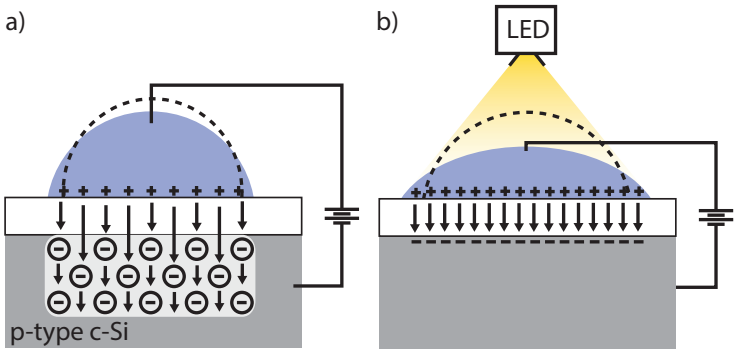

Figure 4.2: The photoelectrowetting effect. a) Initial wetting transition occurs upon application of large negative bias. Dashed line depicts droplet shape prior to application of the bias. Charges in the semiconductor are immobile ionized dopants, depicted as $\ominus$. b) Second wetting transition occurs upon illumination with intense above-bandgap light. Dashed line depicts droplet shape prior to illumination. Charges in the semiconductor are now negative and mobile (electrons).

in the depletion region. Because the illumination is localized to one side of the droplet a gradient in the concentration of minority carriers is established. This gradient is responsible for the force that drives the droplet. However, from diffusion alone we expect this gradient to soften over time and hence for the force to decrease as well. As we saw in the last chapter the time period τ during which the force driving the droplet can be maintained determines the minimum rate of repetition of photoelectrowetting necessary to drive the droplet. However, the problem is not limited to diffusive forces because there is also an electric field working to diminish the concentration gradient of minority carriers. This chapter is an examination of these dynamics via numerical simulations.

In order to study this problem I will examine the case of an MIS capacitor biased into deep-depletion with above-bandgap illumination impinging on the area near one edge. As shown in figure 4.4 the geometry of the capacitor and other simulation parameters are chosen to be comparable to the setup for droplet motion by photoelectrowetting. The absorption coefficient in silicon is approximately $2 \times 10^5\,\mathrm{m}^{-1}$

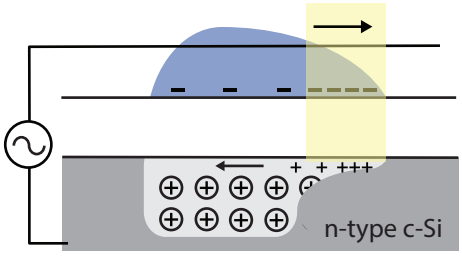

Figure 4.3: Schematic representation for droplet actuation by photoelectrowetting on an n-type silicon wafer. Figure illustrates difference in charge distribution under drop in motion at one instant in time. An asymmetry in the electrowetting is introduced by the photogenerated minority carriers, leading to bulk fluid motion. Arrow indicates direction of motion.

[Palik, 1998] and hence carriers are produced over a region approximately 10 µm deep into the silicon. In photoelectrowetting actuation the depletion region in the unilluminated portions of the droplet grows to upwards of 5 µm[1] and hence the carriers are distributed over the depth of the depletion region when first generated. Once generated these carriers are subject to the electric fields surrounding them and diffusion. The MIS capacitor is a few millimeters in diameter, as are the droplets in the motion experiments presented in this thesis. Given that the depletion width is much smaller then we expect that the minority carriers will migrate to the insulator/silicon interface on short time scales and to the un-illuminated portions of the droplet on longer timescales.

The dynamics of carriers are governed by the set of equations [Roosbroeck, 1950]:

$$\epsilon_s \nabla^2 \phi + e(p - n + N) = 0 \tag{4.1}$$

$$\frac{\partial p}{\partial t} + \nabla \cdot (-\mu_p p \nabla \phi - D_p \nabla p) = 0 \tag{4.2}$$

$$\frac{\partial n}{\partial t} + \nabla \cdot (\mu_n n \nabla \phi - D_n \nabla n) = 0 \tag{4.3}$$

where ϕ is the electric potential, p is concentration of holes and n is the concentration

[1] Calculated using depletion approximation for a bias of 30 V on an n-type sample with resistivity 5 Ω-cm and insulator capacitance of 5.4 F/m.

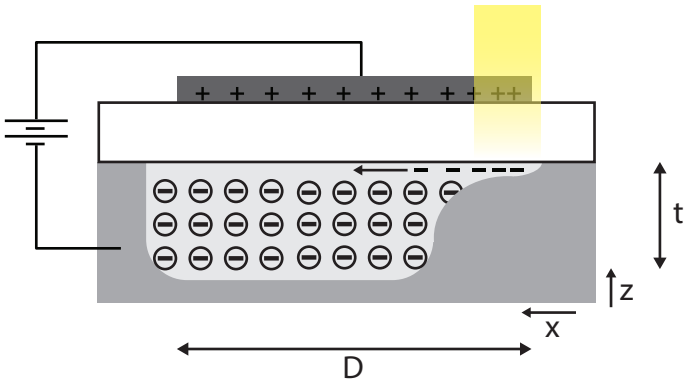

Figure 4.4: Photogenerated carriers in the depletion region of an MIS capacitor, an instant after the electrons have come to the surface. The gate here is made from ITO. The electric field and diffusion tend to equilibrate the concentration of minority carriers across the device. Not to scale, D $\approx 2\,\text{mm}$ and t $\approx 5\,\mu\text{m}$.

of electrons; ϵ_s is the permittivity in the semiconductor, e is the fundamental charge, N is the doping concentration and μ_x, D_x correspond to the mobility and diffusion coefficient for each carrier respectively. Equation 1.10 is Poisson's equation with a term, N, that accounts for the concentration of ionized dopants in a depletion region, fixed in space. Equations 4.2 and 4.3 account for the change in the carrier concentration in response to electric fields and diffusion. Carrier generation in the depletion region is neglected because the minority carrier lifetime is much longer than the periods spanned in the simulations. The solutions to these equations were computed with COMSOL Multiphysics, a finite element package.

4.2 Setup

Equations 4.1 - 4.3 are non-dimensionalized by:

$$\phi \to \phi_0 u \qquad \phi_0 = \frac{kT}{e}$$
$$x \to x_0 \tilde{x} \qquad x_0 = \frac{e^2}{\epsilon_s kT}$$
$$t \to t_0 \tilde{t} \qquad t_0 = \frac{x_0^2}{D_p}$$

where kT is the Boltzmann factor. Using the literature values for these constants and a temperature of 294 K the scalings are $x_0 = 6.11 \times 10^{-8}$ m, $t_0 = 3.20 \times 10^{-12}$ s and $\phi_0 = 25.3$ mV. Employing the Einstein relation $\mu = \frac{kT}{e} D$ and the substitutions above equations 4.1 - 4.3 become:

$$\tilde{\nabla}^2 u + \tilde{p} - \tilde{n} = -\tilde{N} \tag{4.4}$$
$$\frac{\partial \tilde{p}}{\partial \tilde{t}} + \tilde{\nabla} \cdot \left(-\tilde{p} \tilde{\nabla} u - \tilde{\nabla} \tilde{p} \right) = 0 \tag{4.5}$$
$$\beta \frac{\partial \tilde{n}}{\partial \tilde{t}} + \tilde{\nabla} \cdot \left(\tilde{n} \tilde{\nabla} u - \tilde{\nabla} \tilde{n} \right) = 0 \tag{4.6}$$

where all quantities are now dimensionless and $\beta = D_p / D_n$.

The initial conditions, along with the computational domain and boundary conditions are depicted in figure 4.5. The domain is divided into two regions: one corresponding to the semiconductor, labelled 1, and another one corresponding to the insulator, labelled 2. In 2 there are no carriers and u satisfies Laplace's equation $\frac{\epsilon_i}{\epsilon_s} \tilde{\nabla}^2 u = 0$ where ϵ_i is the permittivity of the material. The width of the computational domain is denoted w, the thickness of the semiconductor layer h_1 and the thickness of the insulator h_2. The semiconductor was chosen to be p-type for the simulations.

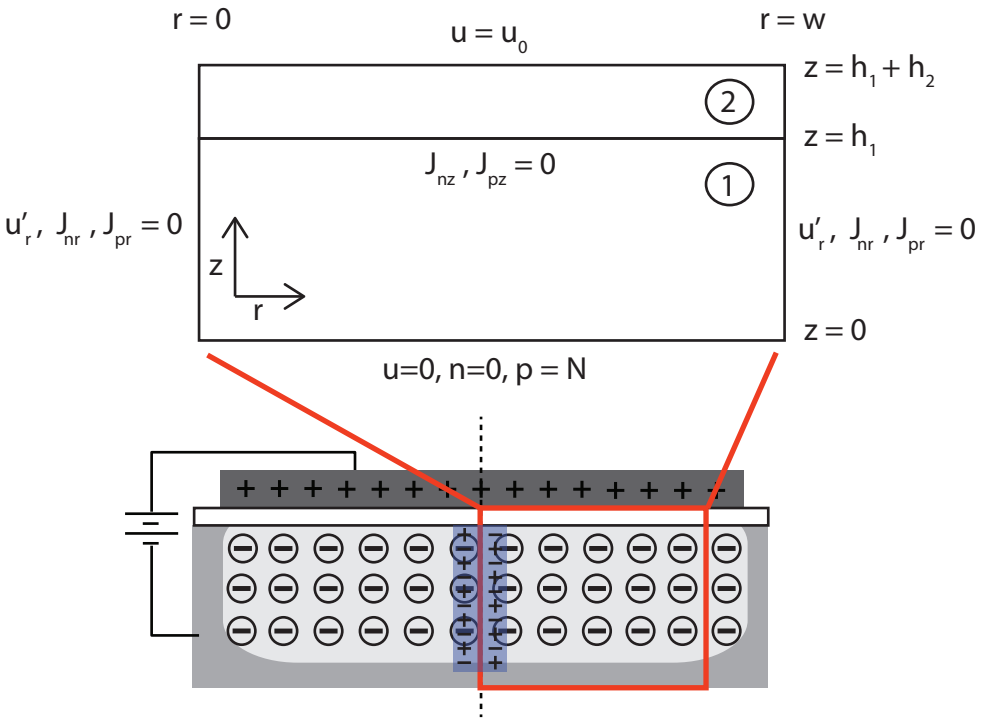

Figure 4.5: Computational domain and boundary conditions. Region labeled 1 is the semiconductor depletion region and region 2 is the insulator. Darker patch in depletion region represents a photo-generated packet of electrons and holes as the initial condition for both carriers. Not to scale; in the simulations $w = 5000$, $h_1 = 150$ & $h_2 = 2$.

The boundary condition at $\tilde{r} = 0$ enforces an axis of rotational symmetry:

$$\partial_r u_r = 0 \tag{4.7}$$

$$J_{nr} = 0 \tag{4.8}$$

$$J_{pr} = 0 \tag{4.9}$$

where $\vec{J_n} = \tilde{n}\tilde{\nabla}u - \tilde{\nabla}\tilde{n}$ and $\vec{J_p} = -\tilde{p}\tilde{\nabla}u - \tilde{\nabla}\tilde{p}$ are the particle fluxes. Hence at $\tilde{r} = 0$, $\tilde{\partial}_r\tilde{n} = 0$ and $\tilde{\partial}_r\tilde{p} = 0$. At $\tilde{r} = w$ the boundary conditions are ill defined and hence I also use equations 4.7 - 4.9 with the understanding that these only apply while the particles are far from the edge.

At $\tilde{z} = h_1$ the particle fluxes are set to zero, $J_{nz}, J_{pz} = 0$, since the carriers cannot penetrate the insulator (region 2). At $\tilde{z} = h_1 + h_2$ the boundary condition $u = u_0$ is set, corresponding to the MIS capacitor gate held at u_0 by the battery. At $\tilde{z} = 0$ $u = 0$, $\tilde{n} = 0$ and $\tilde{p} = |\tilde{N}|$. The condition on u follows from the fact that the silicon bulk is grounded. The condition on $\tilde{n}$ comes from the fact that the device is p-type and $\tilde{n} \ll \tilde{N}$ in moderately doped devices. The $\tilde{z} = 0$ boundary condition on $\tilde{p}$ enforces the equilibrium condition deep into the semiconductor bulk with no electric field and a uniform density of holes, hence $J_p = 0$.

The initial value of $\tilde{n}$ corresponds to a localized packet of electrons as produced by a pulse of light: $\tilde{n}_0 = I_0 e^{-\zeta \tilde{z}} H(\tilde{r} - w_p)$ where $H(x)$ is the Heaviside function, ζ is the absorption coefficient, w_p denotes the extent in the radial direction of the packet of photogenerated charges and I_0 is a constant that determines the total number of particles. The initial value of $\tilde{p}$ is $\tilde{p}_0 = \tilde{p}_{dep} + I_0 e^{-\zeta \tilde{z}} H(\tilde{r} - w_p)$ where $\tilde{p}_{dep}$ is the deep-depletion solution to equations 4.4 - 4.6, obtained by running a simulation with the initial conditions $\tilde{n} = 0$ and $\tilde{p} = |\tilde{N}|$ and extracting the steady state solution for $\tilde{p}$. The solution, $\tilde{p}_{dep}$ is characterized by depletion region where $\tilde{p} = 0$ and a bulk region where $\tilde{p} = |\tilde{N}|$.

4.3 Validation

The model was tested in two scenarios for which there are analytical solutions. First I tested whether the simulation accurately reproduced the depletion zone depth. Next I tested the simulation against an analytical solution for $\tilde{n}$ in the limit $\tilde{n} \ll \tilde{N}$.

4.3.1 Depletion approximation: $\tilde{n} = 0$, $t \to \infty$

This simulation was compared against the well known depletion approximation result [Sze and Ng, 2007] for the width of the depletion region, $W_{dep} \approx \sqrt{\frac{{\epsilon_s}^2}{c_i^2} + \frac{2\epsilon_s V_0}{e|N|}} - \frac{\epsilon_s}{c_i}$. Here $c_i = \frac{\epsilon_i}{h_2}$ is the per unit area capacitance of the insulator. A simulation was

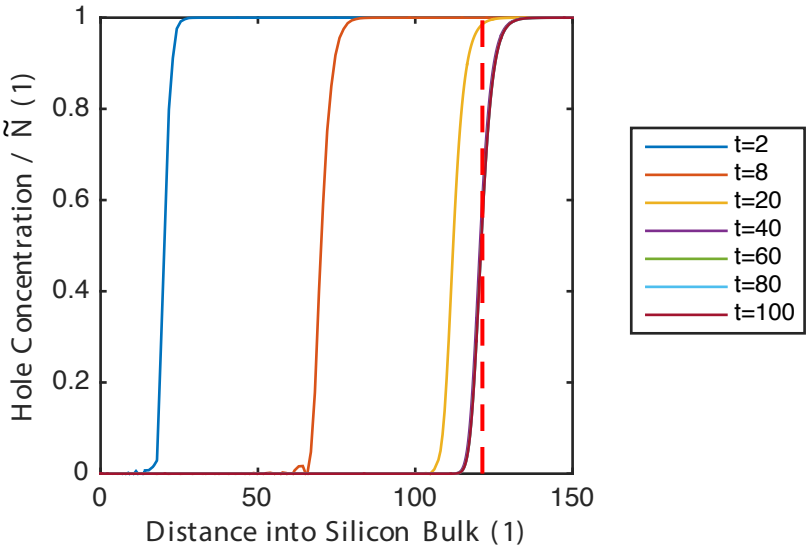

Figure 4.6: Hole concentration in deep-depletion MIS capacitor at different times in a profile of $\tilde{p}$ in the $\tilde{z}$ direction of the computational domain. Figure shows holes receding from semiconductor/insulator interface and settling to a steady state distribution. The left edge corresponds to the top edge of region 1 ($\tilde{z} = h_1$). The red line shows the edge of the depletion region calculated from a depletion approximation analysis. The concentration is shown as a fraction of the acceptor concentration $\tilde{N}$.

run on a p-type material with the initial conditions $n = 0, u = 0$ and $\tilde{p} = |\tilde{N}|$. We set the boundary condition $u_0 = 1600$ and the parameters $w = 10$, $h_1 = 150$, $h_2 = 2$, & $\tilde{N} = 0.18$. A profile of $\tilde{n}(\tilde{r}, \tilde{z}, \tilde{t})$ at $\tilde{r} = 5$ is shown in Fig. 4.6. The simulation shows a depletion region growing away from the interface. At times $\tilde{t} \geq 40$ the edge of the interface converges to the prediction from the depletion approximation.

4.3.2 Limit $\tilde{n} \ll \tilde{N}$, $t \to \infty$

Next the simulation was compared to an analytical solution for $\tilde{n}$ in the limits $\tilde{n} \ll \tilde{N}$ and $\tilde{t} \to \infty$. If electrons are added to the depletion region of a p-type semiconductor these are driven to the insulator/semiconductor interface. If their concentration is insufficient to form the inversion layer the depletion region will persist, with $\tilde{p} = 0$

and the potential satisfying:

$$\partial_{\tilde{z}}^2 u = -\tilde{N} + \tilde{n} \tag{4.10}$$

where the radial component of the Laplacian vanishes, $\partial_{\tilde{r}}^2 u(\tilde{z}) = 0$ if the location is far away from the edge of the capacitor.

In steady state the electron flux in the z direction J_{nz} must vanish:

$$J_{nz} = n\partial_z u - \partial_z n = 0 \tag{4.11}$$

Integrating equation 4.10 in the limit $-\tilde{N} + \tilde{n} \approx -\tilde{N}$ and substituting into equation 4.11 gives:

$$\tilde{n}(-\tilde{N}\tilde{z} + C) = \frac{\partial \tilde{n}}{\partial \tilde{z}} \tag{4.12}$$

where C is a constant. Solving the above:

$$\tilde{n} = \tilde{n}_0 e^{-\frac{\tilde{N}}{2}\tilde{z}^2 + C\tilde{z}} \tag{4.13}$$

where n_0 is a constant.

A simulation was run to test equation 4.13. The initial conditions were $u = 0$, $\tilde{p} = 0$ & $\tilde{n} = 3.32 \times 10^{-8}$ everywhere in the semiconductor. The latter is a small value chosen so that $|\tilde{n}| \ll |\tilde{N}|$ remains valid at all times and for all values of $\tilde{z}$. The boundary conditions were: $u' = 10$, $p = 0$ at $\tilde{z} = 0$ and $u' = 119$ at $\tilde{z} = h_1 + h_2$. The parameters were: $\tilde{N} = 0.18$, $w = 10$, $h_1 = 150$ and $h_2 = 2$. Figure 4.7 shows the simulation correctly converging to the solution given by equation 4.13.

4.4 Simulation & Results

Having validated the simulations with two limiting cases, I next simulated the case of a photo-generated packet of electrons and holes moving in a depletion region,

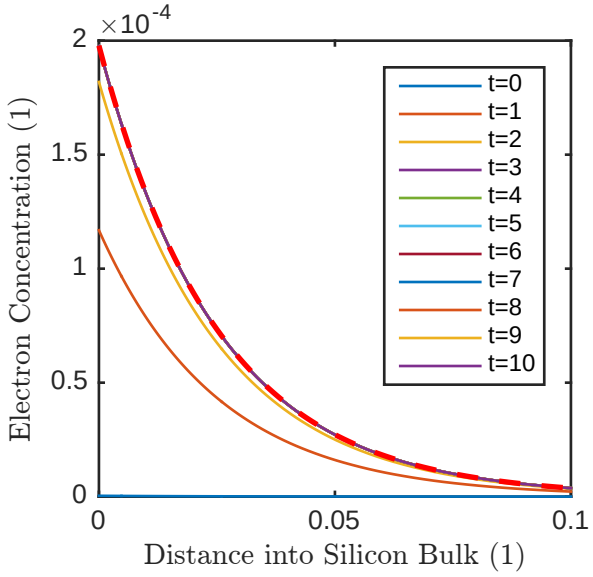

Figure 4.7: Electron concentration at different times in a cutline in the z direction of the computational domain. The figure shows the concentration converging to our analytical estimate, shown as the dashed line.

for general values of $\tilde{n}$ with different concentrations across the depletion region.

Figure 4.8 shows the results of one simulation, for $\tilde{N} = 0.2$, $h_1 = 150$, $h_2 = 2$, w = 5000, $w_p = 200$, and $I_0 = 10$. As shown, this data set exhibits *self-similiarity* [Barenblatt, 1996], that is the solutions at different times can be obtained from another by a transformation of the form $f(\tilde{r}, \tilde{t}) = \tilde{t}^{\alpha} f(\frac{\tilde{r}}{\tilde{t}^{\beta}})$. The parameters α and β were obtained as shown in panels b) and c) by fitting to the general equation for self similar transforms. This yielded for this case $\alpha = 0.6$ and $\beta = 0.4$. The simulation was repeated for different values of $\tilde{N}$ and the results are shown in figure 4.9.

4.5 Discussion

The simulations presented here were undertaken in order to obtain an estimate of the photoelectrowetting cycling frequency necessary for successful actuation. An asymmetry in the concentration of minority carriers across the droplet causes an asymmetry in the electrowetting, resulting in the net force that drives the droplet.

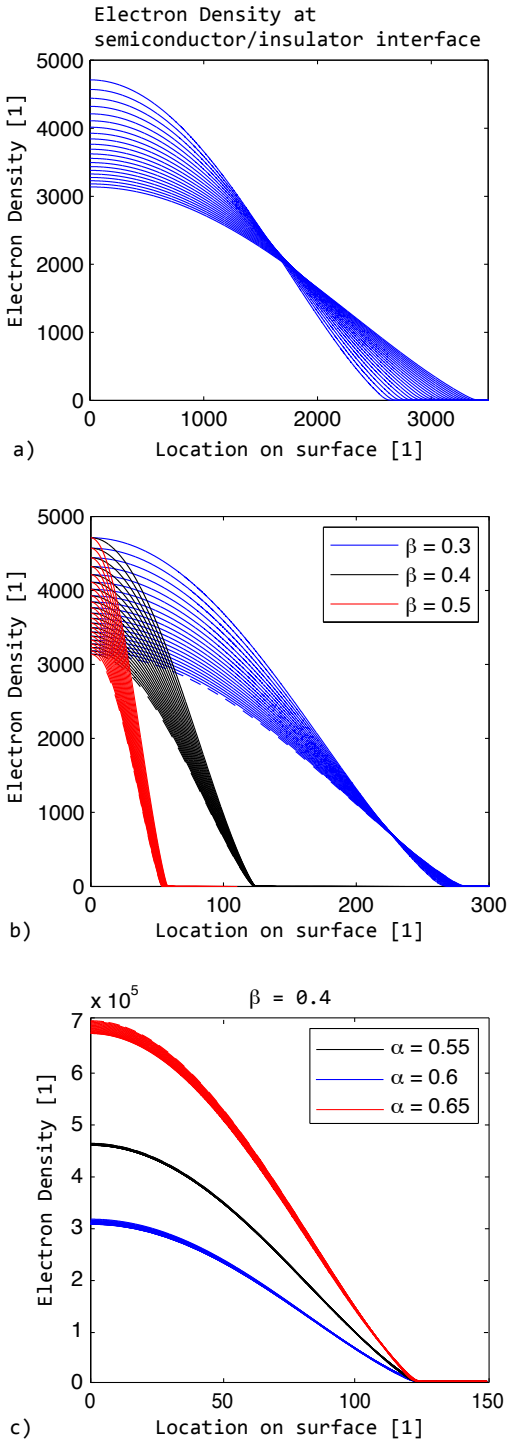

Figure 4.8: a) Raw simulation data from $\tilde{t} = 1000$ to $\tilde{t} = 2000$, for $\tilde{N} = 0.2$, at intervals $\Delta\tilde{t} = 50$. b) Fitting parameter β by inspection. c) Likewise with α.

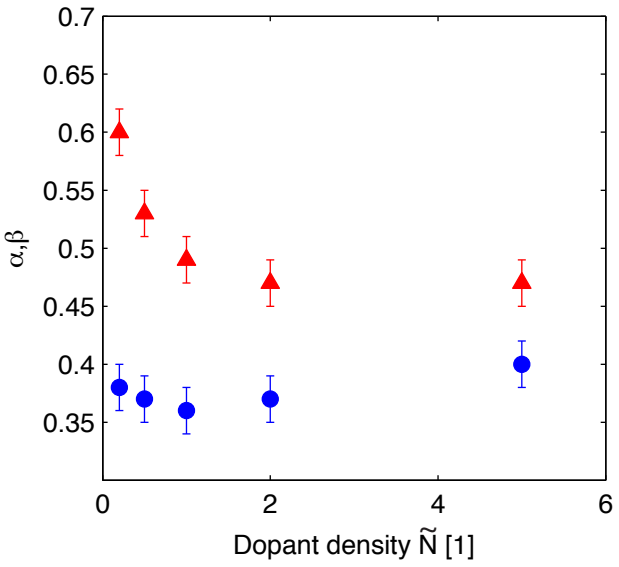

Figure 4.9: Variation in the exponents of similarity transform. The markers ▲ depict values of α and ● depict values of β in the similarity transform $t^{\alpha} f(x/t^{\beta})$

However as discussed previously these minority carriers migrate from the areas in the semiconductor under the beam to the unilluminated regions, breaking the asymmetry. After a period of time τ the concentration of minority carriers is equal on both sides of the semiconductor and the force vanishes. Thus in the periodic forcing scheme demonstrated in chapter III it is necessary to cycle at a frequency $f > 1/2\tau$ in order to force the droplet for a substantial fraction of the time.

In order to obtain an estimate of τ the self-similarity can be exploited as follows. The wavefronts of the distribution follow the power law: $\tilde{t} = k\tilde{r}^{1/\beta}$. The constant k can be extracted from the concentration at a time $\tilde{t}_0$ well into the self-similar regime. Denoting the position of the front $\tilde{r}_0$ then $k = \tilde{t}_0^{\beta}/\tilde{r}_0$. Defining the position of the front as the location where the distribution reaches 1% of its maximum value, as in figure 4.10, this model predicts $\tau \approx 3.7\,\mu s$.

These results are different from the measurements presented in the last chapter, where $\tau \approx 25\,\mu s$. However, it is not possible to make a direct comparison because there were a number of substantial differences between the simulations and the ex-

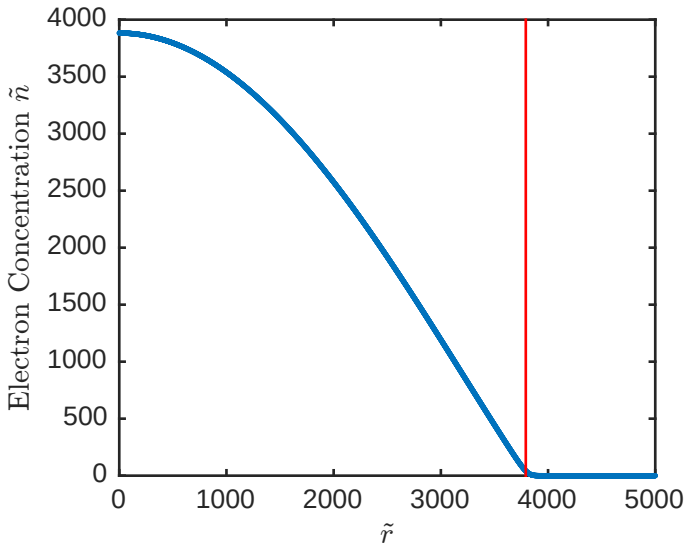

Figure 4.10: Minority carrier concentration at $\tilde{t} = 2911$ in $\tilde{N} = 1$ simulation. Line in red depicts the $\tilde{r}$ value where the distribution meets the threshold value (1%) chosen to define the front.

periment. The simulations were conducted for a device with representative values of the capacitance and gate potential, but not the exact values used in the experiment. Additionally the semiconductor is p-type in the simulations while the experiment was conducted on an n-type device. The mobility of holes is lower by about a factor of 3 compared to electrons, potentially contributing to the discrepancy. Furthermore, as shown in figure 4.12 the measurements were taken with a laser line in order to match the conditions of the photoelectrowetting motion experiments. In contrast the simulations mimic a packet of charge expanding radially outward from the center of the MIS capacitor. Thus the geometry of the experiments is most closely approximated as planar, whereas the simulations are axisymmetric.

A new simulation was conducted with parameters matching the experiment. This simulation was no longer axisymmetric but simply planar. As before τ was calculated using a power law for various distances. The results, as well the data from the τ measurements from chapter III are shown in figure 4.11. Here the three predictions

for τ correspond to different values of the prefactor in the power law. The blue, red and yellow curves correspond to prefactors calculated from threshold values of 1%, 20% and 50% respectively. As the figure shows the agreement is not perfect but the simulation does get the right order of magnitude.

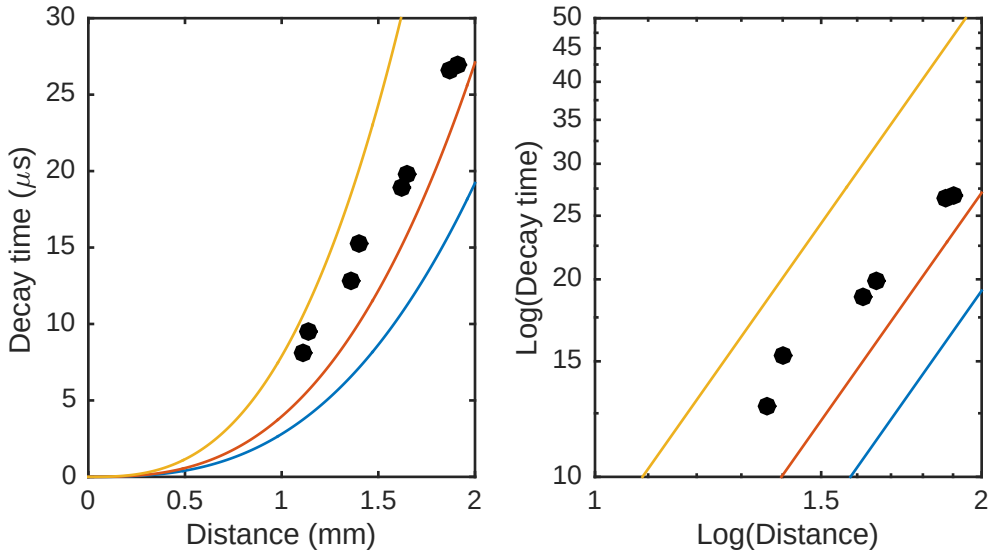

Figure 4.11: Measurement of parameter τ and simulation predictions. Measurements from last chapter are depicted ●. The blue, red and yellow lines are theoretical predictions based on the simulations with different values of the prefactor of the power law as explained in the text.

This difference could arise from mismatch between simulation and experiment. The boundary conditions in the simulation correspond to the charges being far enough from the edge that there is no field in the horizontal direction. In the experiment however, the charges do eventually come close to the edge where there are electric fields in the horizontal direction. Additionally the measurements presented in figure 4.11 are unlikely to arise from a self-similar front because there is some variation in the geometry as the beam is swept across the MIS capacitor for each measurement. Nevertheless the observation of self-similarity, along with experimental confirmation that this model predicts the right order of magnitude demonstrate that the model is

useful for simulating charge distributions in semiconductor depletion regions.

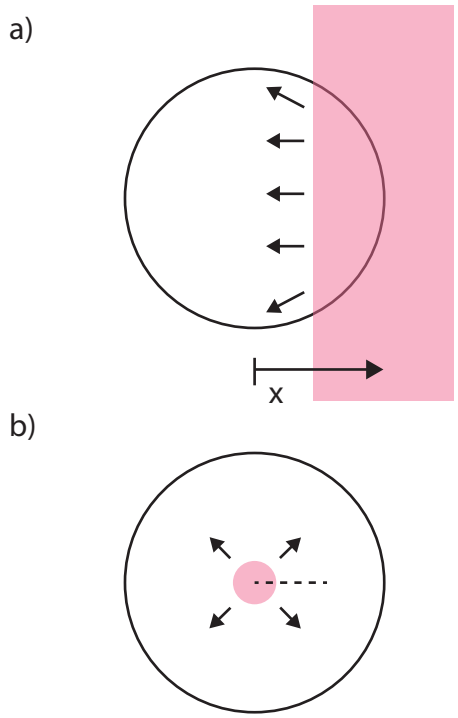

Figure 4.12: a) Top view depiction of setup for τ measurement in chapter III. The circle corresponds to the metal gate of the MIS capacitor. The red patch represents the laser beam and the arrows depict the motion of the photogenerated carriers. Measurements were taken for different values of x, the distance between the center of the MIS capacitor and the beam. b) Top view of simulation. Red circular patch corresponds to distribution of photogenerated carriers at $\tilde{t} = 0$. Dashed line corresponds to computational domain. Not to scale.

4.6 Conclusion

In conclusion numerical simulations were used to predict the motion of minority carriers in depletion regions. The computations were compared to analytical results for limiting cases and shown to be in agreement. In the general case it has been observed that the distributions of minority carriers exhibits self-similarity in the intermediate asymptotic regime. The self-simlar model can be used to predict how

long it takes for carriers to fully invert a surface. The predictions from the self-similar model match well, if not perfectly, with measurements presented in the last chapter.

CHAPTER V

Conclusions

In the introduction to this thesis I postulated that a novel form of electrowetting, photoelectrowetting, could be exploited to actuate translational motion of a sessile droplet using a light beam. The first task in my investigation was to understand the phenomenon of photoelectrowetting and resolve discrepancies between my experimental observations and the literature. To that effect I conducted a comprehensive study of electrowetting-on-semiconductors, from which I concluded:

1. The deformations of the droplet, as quantified by changes in the contact angle, exhibit three regimes corresponding to the charge states of an MIS capacitor: accumulation, deep-depletion and inversion. As shown in figure 2.12, the changes in accumulation and inversion are similar in magnitude, around 30° at 40 V. In contrast the changes in deep-depletion are smaller, around 10° at 40 V.

2. The equilibrium shape of the droplet, and hence the contact angle, is determined by a balance of capillary and electric forces. The contact angle is not accurately predicted by substituting the geometric capacitance in the Young-Lippman equation, c, with the small-signal capacitance of an equivalent MIS capacitor, $\partial Q/\partial V$. In the deep-depletion regime the latter predicts a contact angle change of only 7° in contrast to the observed 20° change.

3. In the deep-depletion regime it is essential to account for interface traps, the fast responding electronic states localized at the semiconductor/insulator interface in order to accurately predict the contact angle. Their inclusion of the model accounts for a 4° correction to the predicted contact angle at 40 V, a 33% increase to the prediction.

4. The light-induced transition is a transition from the meta-stable state deep-depletion to the equilibrium state of inversion. In the experiments reported here this corresponded to a change in the contact angle of 11°.

5. Photoelectrowetting is not reversible by light alone. As shown in figure 2.11 removing the illumination during a photoelectrowetting experiment does not cause the droplet to revert to its pre-illumination shape.

Having elucidated the nature of the light-induced transition I experimented with the actuation scheme depicted in figure 3.4 in order to achieve translational actuation of liquid droplets. From these studies I conclude the following:

1. Translational actuation of liquid droplets is possible with repeated, asymmetric application of the photoelectrowetting effect (see figure 3.3). Speeds of $12\,\mathrm{mm\,s^{-1}}$ were achieved, comparable to traditional electrowetting based devices. Representative values of the experimental parameters are:

    - Cycling frequency: 20 kHz
    - Bias magnitude: 30 V
    - Drop volume: 10 µL
    - Solution composition: Aqueous NaCl (1% w/w) with surfactant SDS (5 mM).
    - Laser intensity: $40\,\mathrm{mW/cm^2}$

2. The cycling frequencies necessary for successful actuation lie in a window determined on the low end by the migration of carriers in the semiconductor from the areas under the beam to the non-illuminated regions under the droplet. As shown in figure 3.11, at a laser intensity of $40\,\mathrm{mW/cm^2}$ this time is around $25\,\mu\mathrm{s}$ for a $10\,\mu\mathrm{L}$ droplet. Hence for a droplet of this size the effect is expected to become significant at frequencies lower than $20\,\mathrm{kHz}$ based on the model of periodic forcing presented here, in agreement with the data presented in figure 3.5. Because it takes a longer time for minority carriers to traverse larger distances the speed is expected to increase with droplet volume in this low frequency regime, as observed in the data of figure 3.8.

3. At higher frequencies the speed is limited by the intensity of the laser which sets the photogeneration rate. Measurements of the contact angle, shown in figure 3.10, indicate a decrease in the force acting on the contact line at a frequency ($\approx 20\,\mathrm{kHz}$) coinciding with a reduction in the speed and the calculated value for the maximum frequency at which the laser fully inverts the semiconductor. Stronger laser intensities increase the speed up to the point that the semiconductor reaches complete inversion (see figure 3.7).

4. Higher biases lead to higher speeds (see figure 3.6), in agreement with the model presented here. In the experiments reported here the speeds ranged from $2\,\mathrm{mm\,s^{-1}}$ at $20\,\mathrm{V_{AC}}$ to $12\,\mathrm{mm\,s^{-1}}$ at $32.5\,\mathrm{V_{AC}}$.

5. Drops with higher viscosities move more slowly (see figure 3.9). In the experiments reported here the speed varied from $14\,\mathrm{mm\,s^{-1}}$ at $1\,\mathrm{mPa\,s}$ to $4\,\mathrm{mm\,s^{-1}}$ at $6\,\mathrm{mPa\,s}$.

As mentioned previously the migration of minority carriers from the illuminated regions of the semiconductor to the non-illuminated regions is a limiting factor for the actuation scheme presented here. Numerical simulations of this phenomenon were

undertaken in order to estimate the photoelectrowetting cycling frequency necessary for successful actuation. From these efforts I conclude:

1. The concentration of minority carriers in depletion regions exhibits self-similarity in time of the form $f(\tilde{r},\tilde{t}) = \tilde{t}^{\alpha} f(\frac{\tilde{r}}{\tilde{t}^{\beta}})$. For the parameters in the simulations presented in chapter IV typical values of α and β were 0.6 and 0.4, respectively.

2. This self-similarity can be used to estimate the concentration of minority carriers in depletion regions over time, as demonstrated in figure 4.11. In the simulations of moderately-doped ($\mathrm{N}_a \approx 1 \times 10^{15}\,\mathrm{cm}^{-3}$) MIS capacitors with geometric capacitance $c \approx 5 \times 10^{-5}\,\mathrm{F/m}^2$ an applied bias of 36 V disperses minority carriers over 2 mm in 3.72 µs.

BIBLIOGRAPHY

BIBLIOGRAPHY

Janelle R Anderson, Daniel T Chiu, Hongkai Wu, OJ Schueller, and George M Whitesides. Fabrication of microfluidic systems in poly (dimethylsiloxane). *Electrophoresis*, 21(1):27–40, 2000.

S. Arscott. Moving liquids with light: Photoelectrowetting on semiconductors. *Scientific reports*, 1, 2011.

Steve Arscott. Electrowetting at a liquid metal-oxide-semiconductor junction. *Applied Physics Letters*, 103(14):144101, 2013.

A Axelevitch, B Gorenstein, and G Golan. Investigation of optical transmission in thin metal films. *Physics Procedia*, 32:1–13, 2012.

Frederick K Balagaddé, Lingchong You, Carl L Hansen, Frances H Arnold, and Stephen R Quake. Long-term monitoring of bacteria undergoing programmed population control in a microchemostat. *Science*, 309(5731):137–140, 2005.

Grigory Isaakovich Barenblatt. *Scaling, self-similarity, and intermediate asymptotics: dimensional analysis and intermediate asymptotics*, volume 14. Cambridge University Press, 1996.

WE Beadle, JCC Tsai, and RD Plummer. *Quick reference manual for silicon integrated circuit technology*. Wiley New York, 1985.

G. Beni and S. Hackwood. Electro-wetting displays. *Applied Physics Letters*, 38: 207–209, 1981.

B Berge. Electrocapillarity and Wetting Of Insulator Films By Water. *Comptes Rendus de L Academie des Sciences Serie Ii*, 317(2):157–163, JUL 22 1993.

B. Berge and J. Peseux. Variable focal lens controlled by an external voltage: An application of electrowetting. *European Physical Journal E*, 3:159–163, 2000.

TD Blake and JM Haynes. Kinetics of liquid/liquid displacement. *Journal of colloid and interface science*, 30(3):421–423, 1969.

Terry D Blake, A Clarke, and EH Stattersfield. An investigation of electrostatic assist in dynamic wetting. *Langmuir*, 16(6):2928–2935, 2000.

Felix Bloch. Über die quantenmechanik der elektronen in kristallgittern. *Zeitschrift für Physik A Hadrons and Nuclei*, 52(7):555–600, 1929.

D. Bonn, J. Eggers, J. Indekeu, J. Meunier, and E. Rolley. Wetting and spreading. *Reviews of Modern Physics*, 81:739–805, 2009.

Emanuel Carrilho, Andres W Martinez, and George M Whitesides. Understanding wax printing: a simple micropatterning process for paper-based microfluidics. *Analytical chemistry*, 81(16):7091–7095, 2009.

Longquan Chen and Elmar Bonaccurso. Electrowetting: From statics to dynamics. *Advances in colloid and interface science*, 210:2–12, 2014.

Stéphanie Chevalliot, Stein Kuiper, and Jason Heikenfeld. Experimental validation of the invariance of electrowetting contact angle saturation. *Journal of Adhesion Science and Technology*, 26(12-17):1909–1930, 2012.

Pei Yu Chiou, Hyejin Moon, Hiroshi Toshiyoshi, Chang-Jin Kim, and Ming C Wu. Light actuation of liquid by optoelectrowetting. *Sensors and actuators A: physical*, 104(3):222–228, 2003.

PY Chiou, Sung-Yong Park, and Ming C Wu. Continuous optoelectrowetting for picoliter droplet manipulation. *Applied Physics Letters*, 93(22):221110, 2008.

Anton A Darhuber, Joseph P Valentino, Sandra M Troian, and Sigurd Wagner. Thermocapillary actuation of droplets on chemically patterned surfaces by programmable microheater arrays. *Journal of Microelectromechanical Systems*, 12(6): 873–879, 2003.

P.-G. de Gennes, F. Brochard-Wyart, and D. Quéré. *Capillarity and Wetting Phenomena: Drops, Bubbles, Pearls, Waves*. Springer, 2004.

Pierre-Gilles De Gennes. Wetting: statics and dynamics. *Reviews of modern physics*, 57(3):827, 1985.

Christelle Decamps and Joël De Coninck. Dynamics of spontaneous spreading under electrowetting conditions. *Langmuir*, 16(26):10150–10153, 2000.

Petra S Dittrich and Andreas Manz. Lab-on-a-chip: microfluidics in drug discovery. *Nature reviews. Drug discovery*, 5(3):210, 2006.

David C Duffy, J Cooper McDonald, Olivier JA Schueller, and George M Whitesides. Rapid prototyping of microfluidic systems in poly (dimethylsiloxane). *Analytical chemistry*, 70(23):4974–4984, 1998.

A Frumkin, A Gorodetskaya, B Kabanov, and N Nekrasov. Electrocapillary phenomena and the wetting of metals by electrolytic solutions, i. *Phys. Z. Sowjetunion*, 1: 255–284, 1932.

A Gorodetskaya and B Kabanov. Electrocapillary phenomena and the wetting of metals by electrolytic solutions, ii. *Phys Z Sowjetunion*, 5:418–431, 1934.

DJ Griffiths. Introduction to electrodynamics. *Upper Saddle River, NJ*, 1999.

AS Grove, BE Deal, EH Snow, and CT Sah. Investigation of thermally oxidised silicon surfaces using metal-oxide-semiconductor structures. *Solid-State Electronics*, 8(2): 145–163, 1965.

Rohini Gupta, Danica M. Sheth, Teno K. Boone, Arianne B. Sevilla, and Joelle Frechette. Impact of pinning of the triple contact line on electrowetting performance. *Langmuir*, 27:14923–14929, 2011.

R. A. Hayes and B. J. Feenstra. Video-speed electronic paper based on electrowetting. *Nature*, 425:383–385, 2003.

Chun Huh and LE Scriven. Hydrodynamic model of steady movement of a solid/liquid/fluid contact line. *Journal of Colloid and Interface Science*, 35(1): 85–101, 1971.

John David Jackson. *Classical Electrodynamics*. John Wiley & Sons, 2007.

Donald R Kerr, Joseph S Logan, P Johannes Burkhardt, and William A Pliskin. Stabilization of sio2 passivation layers with p2o5. *IBM Journal of Research and Development*, 8(4):376–384, 1964.

L. D. Landau and E. M. Lifshitz. *Fluid Mechanics*. Elsevier, 1987.

Nolwenn Le Grand, Adrian Daerr, and Laurent Limat. Shape and motion of drops sliding down an inclined plane. *Journal of Fluid Mechanics*, 541:293–315, 2005.

G. Lippmann. *Relations entre les phénomènes électriques et capillaires*. PhD thesis, Gauthier-Villars, 1875.

Daniel Mark, Stefan Haeberle, Günter Roth, Felix Von Stetten, and Roland Zengerle. Microfluidic lab-on-a-chip platforms: requirements, characteristics and applications. In *Microfluidics Based Microsystems*, pages 305–376. Springer, 2010.

John A Marsh, S Garoff, et al. Dynamic contact angles and hydrodynamics near a moving contact line. *Physical review letters*, 70(18):2778, 1993.

HG Möller. Electrolytic phenomena at the surfaces of electrodes. *Z Phys Chem*, 65: 226–254, 1908.

AR Moore. Electron and hole drift mobility in amorphous silicon. *Applied Physics Letters*, 31(11):762–764, 1977.

F. Mugele and J.-C. Baret. Electrowetting: from basics to applications. *Journal of Physics: Condensed Matter*, 17:R705, 2005.

F. Mugele, A. Klingner, J. Buehrle, D. Steinhauser, and S. Herminghaus. Electrowetting: a convenient way to switchable wettability patterns. *Journal of Physics-Condensed Matter*, 17:S559–S576, 2005.

Yoshiharu Nakamura, Ken'Ichi Kamada, Yoshio Katoh, and Akira Watanabe. Studies on secondary electrocapillary effects. i. the confirmation of youngóduprè equation. *Journal of Colloid and Interface Science*, 44(3):517–524, 1973.

E. H. Nicollian and J. R. Brews. *MOS (Metal Oxide Semiconductor) Physics and Technology*. John Wiley & Sons, New York, 1982.

Edward D Palik. *Handbook of optical constants of solids*, volume 3. Academic press, 1998.

Cesar Palma and Robert Deegan. Electrowetting on semiconductors. *Applied Physics Letters*, 106(1):014106, 2015.

Shao Ning Pei, Justin K Valley, Steven L Neale, Arash Jamshidi, Hsan-Yin Hsu, and Ming C Wu. Light-actuated digital microfluidics for large-scale, parallel manipulation of arbitrarily sized droplets. In *Micro Electro Mechanical Systems (MEMS), 2010 IEEE 23rd International Conference on*, pages 252–255. IEEE, 2010.

Robert F Pierret and Gerold W Neudeck. *Advanced semiconductor fundamentals*, volume 6. Addison-Wesley Reading, MA, 1987.

Robert F Pierret et al. *Semiconductor device fundamentals*. Addison-Wesley Reading, MA, 1996.

M. G. Pollack, R. B. Fair, and A. D. Shenderov. Electrowetting-based actuation of liquid droplets for microfluidic applications. *Applied Physics Letters*, 77:1725–1726, 2000.

Reda R Razouk and Bruce E Deal. Dependence of interface state density on silicon thermal oxidation process variables. *Journal of the Electrochemical Society*, 126(9): 1573–1581, 1979.

Claudio Ronco, A Davenport, and Victor Gura. The future of the artificial kidney: moving towards wearable and miniaturized devices. *Nefrologia*, 31(1):9–16, 2011.

W Van Roosbroeck. Theory of the flow of electrons and holes in germanium and other semiconductors. *Bell Labs Technical Journal*, 29(4):560–607, 1950.

Kee Scholten, Xudong Fan, and Edward T Zellers. A microfabricated optofluidic ring resonator for sensitive, high-speed detection of volatile organic compounds. *Lab on a Chip*, 14(19):3873–3880, 2014.

Ralf Seemann, Martin Brinkmann, Thomas Pfohl, and Stephan Herminghaus. Droplet based microfluidics. *Reports on progress in physics*, 75(1):016601, 2011.

DL Staebler and CR Wronski. Reversible conductivity changes in discharge-produced amorphous si. *Applied physics letters*, 31(4):292–294, 1977.

Howard A Stone, Abraham D Stroock, and Armand Ajdari. Engineering flows in small devices: microfluidics toward a lab-on-a-chip. *Annu. Rev. Fluid Mech.*, 36: 381–411, 2004.

S.M. Sze and Kwok K. Ng. *Physics of semiconductor devices*. Wiley, New York, 2$^{\text{nd}}$ edition, 2007.

Shia-Yen Teh, Robert Lin, Lung-Hsin Hung, and Abraham P Lee. Droplet microfluidics. *Lab on a Chip*, 8(2):198–220, 2008.

Todd Thorsen, Sebastian J Maerkl, and Stephen R Quake. Microfluidic large-scale integration. *Science*, 298(5593):580–584, 2002.

George M Whitesides. The origins and the future of microfluidics. *Nature*, 442(7101): 368–373, 2006.

Paul Yager, Thayne Edwards, Elain Fu, Kristen Helton, Kjell Nelson, Milton R Tam, and Bernhard H Weigl. Microfluidic diagnostic technologies for global public health. *Nature*, 442(7101):412, 2006.

Leslie Y Yeo and James R Friend. Ultrafast microfluidics using surface acoustic waves. *Biomicrofluidics*, 3(1):012002, 2009.

Thomas Young. An essay on the cohesion of fluids. *Philosophical Transactions of the Royal Society of London*, 95:65–87, 1805.